Point Vortex Models for Modon Dynamics

Thesis by

Dana Hobson

In Partial Fulfillment of the Requirements

for the Degree of

Doctor of Philosophy

California Institute of Technology

Pasadena, California

June, 1991

(Submitted 28 August 1990)

Acknowledgments

I would like to thank my advisor, Professor Philip Saffman, for his reliable advice, patience, and encouragement during my time as a student.

I would like to thank fellow students, Julian Anthony, Roberto Camassa, Tasso Kaper, Gregor Kovacic, Vered Rom-Kedar, and Israel Soibelman. I am thankful for their friendship and advice. I would also like to thank Jim Buntine, Kirk Brattkus, and Barry Ryan who read parts of the thesis and made helpful suggestions.

I gratefully acknowledge a fellowship from the Hertz Foundation which accounted for the major portion of my financial support. I also thank Caltech and the Department of Energy for additional support under grant DE-FG03-89ER25073.

Finally, I would like to thank my mother, Edna Hobson, for her support throughout my education and Eli Herrera for her support during my graduate years.

Abstract

We study the dynamics of modons in the Charney-Hasegawa-Mima equation using a point vortex model introduced by Zabusky and McWilliams. This model reduces the equation to a system of ordinary differential equations which facilitate systematic studies of several problems involving modons. These problems are relevant to the study of large-scale motions in the Earth's atmosphere as well as the study of microturbulence in tokamak plasmas. We study the possible motions of an isolated modon using the model and show by direct numerical simulation that these motions compare very well with those of actual modons. As a by-product, we discover that the path of a left-moving (westward) modon is actually unstable to small perturbations in its position or orientation. This points out that a modon may be unstable in the path sense even if it is stable in the Lyapunov sense, as was shown for left-moving modons by Laedke and Spatschek. We use the flow field generated by the model to study the flow of fluid around an isolated modon. We show that the separatrices enclosing a modon in uniform motion break and tangle in the fashion described by Poincare when the motion is nonuniform. This is established analytically by computation of a Melnikov integral and numerically by plotting invariant manifolds of stagnation points in the flow. In contrast to past assumption, we find that significant mixing occurs between the modon and the external flow when the modon is not in uniform motion. So, at least on long timescales, modons do not serve as complete atmospheric blocks. Finally, we apply the model to the study of coaxial collisions between two modons. This results in a problem for the motion of four point vortices similar to that considered by Love for point vortices in the Euler equations. The relative behavior of the two modons is described completely by a planar Hamiltonian system which we study in detail. We find a wide variety of possible interactions between the two modons and note several behaviors not previously observed in numerical simulations. An effort is made to relate these results to the fluid inside a tokamak which may contain many such modons with frequent collisions.

Table of Contents

List of Figures

CHAPTER 1

INTRODUCTION

In this thesis we study the dynamics of a certain coherent structure, known as a 'modon' or Rossby soliton, found in the Charney-Hasegawa-Mima (or CHM) equation (Charney [1948], Hasegawa and Mima [1977], [1978]) for $\psi(x, y, t)$:

$$(\nabla^2\psi - \gamma^2\psi)_t + [\psi, \nabla^2\psi] + \beta\psi_x = 0.$$

The subscripts denote differentiation and the bracket is the Jacobian $[A, B] = A_xB_y - A_yB_x$. The parameters γ and β are positive constants. This equation arises in the study of large-scale motions in the Earth's atmosphere when the β-plane approximation is used (see Pedlosky [1979]). The domain is a plane tangent to the Earth's surface where x and y represent east and north respectively and ψ is the streamfunction for the atmosphere. It also applies to low frequency magnetized plasmas, which are found in tokamak plasma confinement devices (see Liewer [1985] or Hasegawa, Maclennan, and Kodama [1979]). In this case, the domain is the plane perpendicular to the magnetic field, which points along the axis of the toroidal device, and ψ is the electric potential of the plasma inside.

The coherent structure is realized in special cases as an exact traveling wave solution, generally referred to as the modon solution to the CHM equation. A detailed derivation may be found in Larichev and Reznik [1976]. This solution is of the form $\psi(x,y,t)=\Psi(x-Ut,y)$. The function Ψ can be expressed as

$$\Psi=-aU\Big((1+\frac{p^2}{q^2})\frac{r}{a}-\frac{p^2}{q^2}\frac{J_1(qr/a)}{J_1(q)}\Big)\sin\theta \qquad\qquad r<a$$

and

$$\Psi=-aU\frac{K_1(pr/a)}{K_1(p)}\sin\theta \qquad\qquad r>a$$

where r and θ are polar coordinates, J_1 and K_1 are Bessel functions and a is an arbitrary parameter refered to as the modon radius. The parameter p is given by $p^2=a^2(\gamma^2+\beta/U)$ and the parameter q must satisfy the eigenvalue problem

$$\frac{1}{p}\frac{K_1'(p)}{K_1(p)}+\frac{1}{q}\frac{J_1'(q)}{J_1(q)}=\frac{1}{p^2}+\frac{1}{q^2}.$$

This eigenvalue problem has a countable infinity of positive solutions q for each given positive p. In all cases we choose the 'ground state modon' by taking the smallest positive q. The speed U must lie outside the interval $(-\beta/\gamma^2,0)$ so that p is real, but is arbitrary otherwise. The solution so constructed makes ψ, $\nabla\psi$, and $\nabla^2\psi$ continuous but has a jump discontinuity in the third radial derivative of ψ at $r=a$. The modon is strongly isolated in space owing to the exponential decay of $K_1(z)$ for large z.

Although no exact solutions exist for modons in nonuniform motion, numerical simulations show that such strongly isolated coherent dipolar structures can exist in a variety of circumstances. An initial distribution given by $\psi(x,y,0)=\Psi(x,y)$ above for some U and a will evolve under the CHM equation as a coherent structure traveling horizontally at constant speed (McWilliams *et al.* [1981]). An initial distribution corresponding to the modon solution tilted at a small angle evolves as a wobbling coherent dipole (Makino, Kamimura, and Taniuti [1981]). The modon oscillates vertically about its initial horizontal position while wobbling and propagating horizontally. Two modons can also collide with one another, returning roughly to their original shapes and speeds after the interaction (McWilliams and Zabusky [1982]). These collisions are, however, neither conservative nor coherent in general (Larichev and Reznik [1983]).

A great deal of work has concentrated on the stability of modons. Laedke and Spatschek [1985] established that modons moving to the left at constant speed (westward modons) are neutrally stable to infinitesimal perturbations in the Lyapunov sense. Sakuma and Ghil [1990] proved a similar result for the original stationary modon solution due to Stern [1975]. Similar proofs of stability for right-moving modons were shown to be in error (Carnevale *et al.* [1988b]). Several numerical studies have shown that modons are stable to sufficiently small topographic perturbations, but will break up for large perturbations (McWilliams *et al.* [1981] and Carnevale *et al.* [1988a]). Even in the absence of complete analytical proof, modons are generally believed to be neutrally stable and to move coherently, retaining their dipolar structure and strong spatial isolation.

The presence of such a stable, isolated structure in the CHM equation has relevance to both the atmospheric and plasma applications. It is believed that modons may provide a mechanism for atmospheric blocking (Verkley [1989]). This occurs when westerly flows in the north Atlantic are split into two streams and diverted around a large stable disturbance of different character than the main flow. Such disturbances have been observed repeatedly, occuppying roughly 45 degrees of latitude with durations ranging from two days to two weeks. The shape of such disturbances, as well as the length and time scales involved, are consistent with the assumptions made in deriving the CHM equation for atmospheric disturbances. Thus, modons are natural candidates for atmospheric blocks. It is then interesting to study the dynamics of an isolated modon and its ability to divert or block an external flow.

The presence of modons has several important implications for tokamak plasmas. Since modons are coherent structures, they can slow or stop the inverse cascade of energy to long wavelengths observed in such plasmas (Fischer and Kramer [1989]). If modons form in the plasma, energy will be trapped at wavelengths roughly equal to the typical radius of the modons present. The formation of stable dipolar structures has been observed in similar plasmas (Pecseli *et al.* [1984]). These highly nonlinear disturbances could also greatly alter the transport properties of the plasma, perhaps accounting for the anomalous transport observed in tokamaks (Yu and Lisak [1986] and Jovanovic [1988]).

Although the CHM equation itself does not address transport in the plasma (Liewer [1985]), it does serve as a simple canonical equation for more general equations which do address transport. Equations similar to the CHM which take into account variation along the magnetic field (Shukla, Spatschek, and Balescu [1985]), plasma rotation (Shukla and Yu [1986] and Horton *et al.* [1986]), magnetic shear, and other phenomena (see for example Mikhailovskii *et al.* [1984]) have been shown to possess a dipole-vortex solution similar to the modon. Yu and Lisak [1986] showed that such solutions are generic to inhomogeneous magnetized plasmas, as are found in tokamaks. So, an understanding of the consequences of the presence of modons in the CHM equation could help to understand how such structures affect transport. In this respect, it is interesting to study the dynamics of individual modons and their behavior in collisions with other modons.

Owing to the complicated nature of the CHM equation and the nonlinear structure of the modon, we have chosen in this thesis to study problems relating to the applications using a point vortex model. In brief, we replace a modon by two point vortices of equal and opposite strength. We then follow the evolution of such dipoles by deriving equations for the point vortices consistent with the CHM equation. Thus the study of modon dynamics is reduced to the study of a set of ordinary differential equations. This has allowed us to perform systematic studies of three problems concerning modons. First we study the dynamics of a single, isolated modon using the model. This results in a simple planar system from which the possible motions of the modon can be determined. We compare these motions with those obtained from direct numerical simulations of the CHM equation to establish the utility of the model. We then study the flow of fluid around the modon to show that the fluid inside the modon mixes with the external flow in general, showing that the modon is not a complete atmospheric block. Finally, we study coaxial collisions between two modons using the model. The resulting system reduces to a complicated planar system which we analyze in detail. We find many possible interactions and note ones that were not expected from looking at previous numerical simulations of modon collisions.

CHAPTER 2

Point Vortex Dipole Model of an Isolated Modon

2.1 Introduction

In this chapter we develop and study a point vortex dipole model of an isolated modon. Our intentions are to find all the possible behaviors of a single modon and to develop a model which can be used to study more complicated problems involving modons. This has direct application to the problem of atmospheric blocking, where the knowledge of the behavior of a single modon depending upon its orientation may be relevant. Also, a successful model would be useful in simulating the dynamics of a fluid with many modons, as a tokamak plasma is believed to be.

We first give the point vortex formulation of the CHM equation due to Zabusky and McWilliams [1982]. We use this formulation to model the modon with a dipole consisting of two point vortices of equal and opposite strength. The motion of this dipole can be described by a planar Hamiltonian system of ordinary differential equations. We study the phase plane of this system for various parameter values to reveal the qualitative behaviors exhibited by the dipole.

We find uniform motion in which the dipole propagates horizontally or is stationary. Small and moderate amplitude nonuniform motions about some of these uniform states are families of 'wobbling' motions in which the inclination of the dipole oscillates while propagating horizontally. Larger amplitude motions include families of 'tumbling' motions in which the dipole rolls while propagating along a path resembling a cycloid.

We show that the parameters in the model can be chosen to match the speed and far-field behavior of a given modon in uniform motion, provided the modon is sufficiently small and fast. We then choose the parameters specifying a dipole to model a given modon in order to compare the behavior of the two when placed in nonuniform motion. We find that the period and average speed of the dipole and modon in the periodic wobbling motion are in excellent qualitative agreement, while the quantitative agreement is somewhat rough.

A study of the uniform motions reveals that a left-moving dipole is unstable in the sense that its path can be pushed into a finite amplitude orbit by an arbitrarily small perturbation of its height or inclination. We confirm this surprising prediction for the modon by direct numerical simulation. This result sheds new light on the stability proofs for left-moving and stationary modons due to Laedke and Spatschek [1985] and Sakuma and Ghil [1990] respectively.. A right-moving dipole is stable in the path sense, being pushed into small-amplitude wobbling by small perturbations.

2.2 Point Vortex Model

In this section we present the point vortex model of Zabusky and McWilliams [1982]. This model is similar to the well-known point vortex formulation of the two-dimensional Euler equations (Aref and Pomphrey [1982]). We will use this model throughout this thesis to reduce the study of modon motions to the study of relatively simple sets of ordinary differential equations.

The heart of the model is its interpretation of the CHM equation

$$(\nabla^2\psi - \gamma^2\psi)_t + [\psi, \nabla^2\psi] + \beta\psi_x = 0 \tag{2.1}$$

as an equation for the rate of change of $\kappa = \nabla^2\psi - \gamma^2\psi$ along streamlines. The quantity κ is assumed to be concentrated at discrete points in the plane,

$$\kappa = \sum_i \kappa_i(t)\delta(\mathbf{x} - \mathbf{x}_i(t))$$

where $\kappa_i(t)$ is the strength and $\mathbf{x}_i(t) = (x_i(t), y_i(t))$ is the position of the i^{th} point vortex. Dynamical equations for the strength and position of each vortex are then given.

The point vortex model assumes that each vortex moves with the velocity induced by all the other vortices. A vortex does not induce a velocity on itself. The streamfunction due to each point vortex must be consistent with the singular distribution of κ in the vortex. Thus the stream function ψ_j for the j^{th} vortex must satisfy $\nabla^2\psi_j - \gamma^2\psi_j = \kappa_j\delta(\mathbf{x} - \mathbf{x}_j(t))$. The stream function is then proportional to the Green function for the operator $\nabla^2 - \gamma^2$, so

$$\psi_j = \frac{-\kappa_j}{2\pi} K_0(\gamma|\mathbf{x} - \mathbf{x}_j|) \tag{2.2}$$

where K_0 is the modified Bessel function of the second kind. The velocity field induced by the j^{th} vortex is given by $\mathbf{v}_j = (u_j, v_j) = (-\partial_y\psi_j, \partial_x\psi_j)$. The velocity of the i^{th} vortex is the sum of the velocities contributed by each of the other vortices at the point (x_i, y_i). So, taking the partial derivatives of the expression for the stream function above, we see that the i^{th} vortex moves according to

$$(\dot{x}_i, \dot{y}_i) = \frac{\gamma^2}{2\pi} \sum_{j \neq i} \kappa_j \frac{K_1(\gamma|\mathbf{x}_i - \mathbf{x}_j|)}{(\gamma|\mathbf{x}_i - \mathbf{x}_j|)} (y_j - y_i, x_i - x_j). \tag{2.3}$$

This expression specifies the motion of each vortex in terms of the positions of the other vortices and their strengths. The time dependence of the strengths κ_i is obtained by rewriting (2.1) as

$$\kappa_t + \hat{z} \times \nabla\psi \cdot \nabla\kappa = -\beta\psi_x. \tag{2.4}$$

The term on the left side of (2.4) is just the rate of change of κ along streamlines since $\hat{z} \times \nabla\psi$ is the velocity of the fluid. The term on the right side of (2.4) is $-\beta$ times the y component of the velocity. In terms of the point vortex distribution, this is interpreted as meaning that the time rate of change of the strength of a point vortex is equal to $-\beta$ times the y component of its velocity, *i.e.*

$$\dot{\kappa}_i = -\beta\dot{y}_i.$$

This can be integrated to give

$$\kappa_i = q_i - \beta y \tag{2.5}$$

where $q_i = \kappa_i^0 + y_i^0$. Recall that the quantity $q = \kappa + \beta y$ is the potential vorticity and is constant along streamlines according to (2.1).

Equations (2.3) and (2.5) give a complete prescription for evolving a set of point vortices in a fashion consistent with the CHM equation. We have been unable to show that these equations form a Hamiltonian system, as is the case for the Euler equation point vortices (Aref and Pomphrey [1982]). Nevertheless, we will show that it is a good model for modon motions in a certain parameter range and we will go on to use it to study various aspects related to modon motions. In each special case studied we have been able to find a Hamiltonian for the system, so the lack of a Hamiltonian for the general system has not hampered us. We stress that this is intended only as a model for the coherent motion of vortices in the CHM equation. This is not a weak solution for the CHM equation, unlike the point vortex formulation of the two-dimensional Euler equations.

2.3 Dipole Model of Modon

In this section we apply the point vortex model of the previous section to model the motion of a single modon. We replace the modon's dipolar distribution of vorticity by a dipole of finite size consisting of a pair of point vortices of equal and opposite strength. The motion of this dipole is meant to model the motion of the modon. The two point vortices are set apart a finite distance so that their separation is roughly equal to that between the centers of the monopolar vortices in the modon. This results in a set of ordinary differential equations for the paths of these point vortices which are relatively easy to analyze. We reduce these equations to a planar system which can be solved in closed form. We analyze all the solutions of this system and infer all the possible motions exhibited by this dipole model.

2.3.1 Equations of motion for two point vortices

The general problem we consider is illustrated in Figure 2.1. We follow the evolution of the cartesian coordinates for the positions of two point vortices. The coordinates of the point vortices are (x_1, y_1) and (x_2, y_2) respectively. The vortices have strengths κ_1 and κ_2 respectively. We center the coordinate system so that the vortices are initially reflections of one another through the origin. The constants x_0 and y_0 are the initial x and y distances of the vortices from the origin of the coordinate system. In order to model a dipole we make the strengths initially equal and opposite, so that $\kappa_2 = -\kappa_1$. As a consequence of the evolution equations

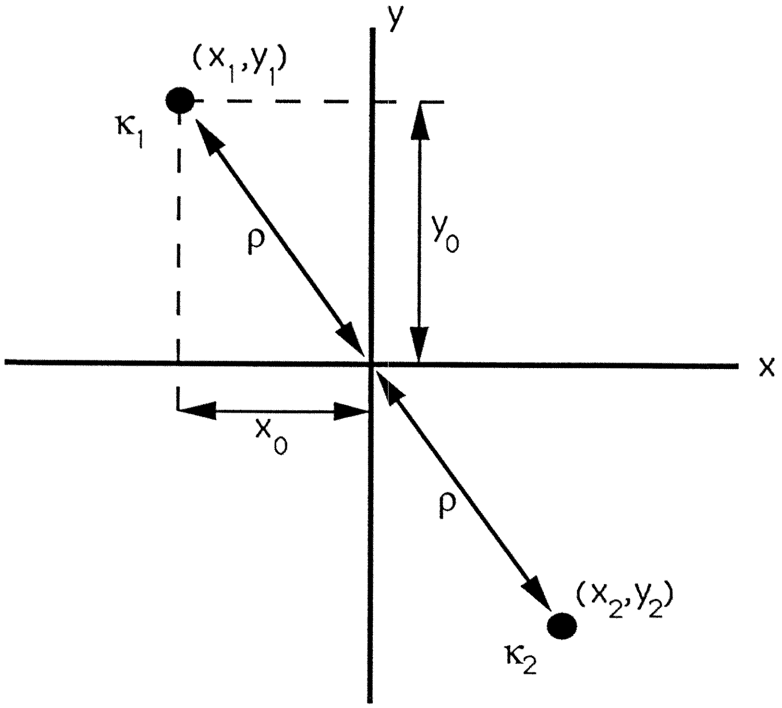

Figure 2.1 Geometry of the two point vortex problem.

for the strengths, this equality holds for all time. So, we take $\kappa_1 = -\kappa_2 = \kappa_0$, where κ_0 is constant.

The evolution equations from (2.3) for the positions of the point vortices are

$$\begin{aligned} \frac{dx_1}{dt} &= \frac{\gamma\beta}{2\pi}\frac{K_1(2\gamma\rho)}{2\rho}(\delta + y_2)(y_1 - y_2) \\ \frac{dy_1}{dt} &= -\frac{\gamma\beta}{2\pi}\frac{K_1(2\gamma\rho)}{2\rho}(\delta + y_2)(x_1 - x_2) \\ \frac{dx_2}{dt} &= \frac{\gamma\beta}{2\pi}\frac{K_1(2\gamma\rho)}{2\rho}(\delta - y_1)(y_1 - y_2) \\ \frac{dy_2}{dt} &= -\frac{\gamma\beta}{2\pi}\frac{K_1(2\gamma\rho)}{2\rho}(\delta - y_1)(x_1 - x_2) \end{aligned} \tag{2.6}$$

with initial conditions $x_1(0) = -x_0$, $y_1(0) = y_0$, $x_2(0) = x_0$, and $y_2(0) = -y_0$. In the above K_1 is a modified Bessel function of the second kind and the quantities δ and ρ are defined as follows :

$$\delta = \frac{\kappa_0}{\beta} + y_0$$

$$\rho = \frac{1}{2}((x_1 - x_2)^2 + (y_1 - y_2)^2)^{\frac{1}{2}}.$$

The quantity ρ is the half-distance between the vortices and δ is a measure of the overall strength of the vortices. The constants x_0 and y_0 may take on any values between $-\rho$ and ρ, representing arbitrary initial configurations of the two point vortices. Without loss of generality, we take ρ and κ_0 to be positive. Since $y_0 > -\rho$, the parameter δ must satisfy $\delta > -\rho$.

2.3.2 Reduction of the equations of motion to a planar system

We can reduce the system (2.6) to a form which is simpler to analyze by making a series of observations and transformations. We start by using the scaled time

$$\tau = \frac{\gamma\beta}{\pi}\frac{K_1(2\gamma\rho)}{2\rho}t.$$

We follow Zabusky and McWilliams [1982] in defining centered coordinates

$$\bar{x} = \frac{1}{2}(x_1 + x_2) \qquad \xi = \frac{1}{2}(x_1 - x_2)$$

$$\bar{y} = \frac{1}{2}(y_1 + y_2) \qquad \eta = \frac{1}{2}(y_1 - y_2).$$

The resulting equations are

$$\frac{d\bar{x}}{d\tau} = (\delta - \eta)\eta \qquad \frac{d\xi}{d\tau} = \bar{y}\eta$$

$$\frac{d\bar{y}}{d\tau} = -(\delta - \eta)\xi \qquad \frac{d\eta}{d\tau} = -\bar{y}\xi.$$

In these variables $\rho^2 = \xi^2 + \eta^2$.

We note that ρ is conserved since $\rho\dot{\rho} = \xi\dot{\xi} + \eta\dot{\eta} = 0$. The polar coordinate representation

$$\xi = \rho\cos\theta \qquad \eta = \rho\sin\theta$$

takes advantage of this conserved quantity explicitly. The resulting system of equations is given by

$$\frac{d\bar{y}}{d\tau} = \frac{\partial H}{\partial\theta} = -\rho\cos\theta(\delta - \rho\sin\theta) \tag{2.7a}$$

$$\frac{d\theta}{d\tau} = -\frac{\partial H}{\partial \bar{y}} = -\bar{y} \tag{2.7b}$$

$$\frac{d\bar{x}}{d\tau} = \rho \sin\theta(\delta - \rho\sin\theta) \tag{2.8}$$

where ρ is constant at its initial value $\rho = \sqrt{x_0^2 + y_0^2}$. The variables $\bar{y}$ and θ form a planar Hamiltonian system with Hamiltonian

$$H = \frac{1}{2}\bar{y}^2 - \rho\delta\sin\theta + \frac{1}{2}\rho^2\sin^2\theta - \frac{1}{4}\rho^2. \tag{2.9}$$

The equation for $\bar{x}$ decouples from this system and can be solved by quadrature using the formula

$$\bar{x}(\tau) = \bar{x}(\tau_0) + \rho\int_{\tau_0}^{\tau}(\delta - \rho\sin\theta(s))\sin\theta(s)ds. \tag{2.10}$$

So the problem of determining the evolution of the positions of the two point vortices reduces to solving the planar system (2.7) with Hamiltonian (2.8) and parameters ρ and δ. We study the qualitative behavior of (2.7) in the next subsection. The system can be integrated completely in terms of elliptic functions which we demonstrate in the appendix.

2.3.3 Phase plane analysis of the planar system

The qualitative behavior of the system (2.7) can be studied by constructing the phase portraits of the system for various values of the parameters. Below we discuss the fixed points of the system and their stability. We use this information and the value of the Hamiltonian at each fixed point to determine the qualitative structure of the phase portraits.

A few general observations about the system (2.7) are useful. First, the system is 2π–periodic in θ and we have chosen $[-\pi/2, 3\pi/2)$ as a sample interval for convenience. Second, the qualitative behavior depends only on the ratio δ/ρ, not on δ and ρ separately. Since $\delta > -\rho$ this ratio must satisfy $\delta/\rho > -1$. Finally, all fixed points must have $\bar{y} = 0$. So, we can simplify various expressions to their values at $\bar{y} = 0$. The equation for the value of θ at a fixed point becomes

$$\cos\theta(\sin\theta - \frac{\delta}{\rho}) = 0.$$

The Hamiltonian H evaluated at $\bar{y} = 0$ is

$$H = \rho^2(\frac{1}{2}\sin^2\theta - \frac{\delta}{\rho}\sin\theta - \frac{1}{4}).$$

The Jacobian $J = H_{\theta\theta}H_{\bar{y}\bar{y}} - H^2_{\bar{y}\theta}$ evaluated at $\bar{y} = 0$ is

$$J = \rho^2(\frac{\delta}{\rho}\sin\theta + 1 - 2\sin^2\theta).$$

The sign of J at a fixed point determines the stability of the fixed point. If $J > 0$ the fixed point is a center and if $J < 0$ it is a saddle. The value of H at the fixed points will determine how the separatrices of the saddles lie in relation to one another.

One set of fixed points satisfies $\cos\theta = 0$. The two values of θ in the interval $[-\pi/2, 3\pi/2)$ satisfying this are $\theta = -\pi/2$ and $\theta = \pi/2$. At $\theta = -\pi/2$, $H = \rho^2(\delta/\rho + 1/4)$ and $J = -\rho^2(1+\delta/\rho)$. This fixed point is always a saddle since $J < 0$ for all $\delta/\rho > -1$. At $\theta = \pi/2$, $H = \rho^2(1/4 - \delta/\rho)$ and $J = \rho^2(\delta/\rho - 1)$. This fixed point is a saddle for $\delta/\rho < 1$, since $J < 0$ there, and a center for $\delta/\rho > 1$.

For $\delta/\rho < 1$ there are saddles at $\theta = \pm\pi/2$, each giving rise to separatrices in the phase portrait. The value of the Hamiltonian at each saddle determines the relationship between these separatrices. For $\delta/\rho < 0$, $H(\pi/2) > H(-\pi/2)$ so the separatrix emanating from $\theta = \pi/2$ lies outside, or encloses, the separatrix emanating from $\theta = -\pi/2$. For $\delta/\rho > 0$, $H(-\pi/2) > H(\pi/2)$ so the separatrix from $\theta = -\pi/2$ lies outside the one from $\theta = \pi/2$.

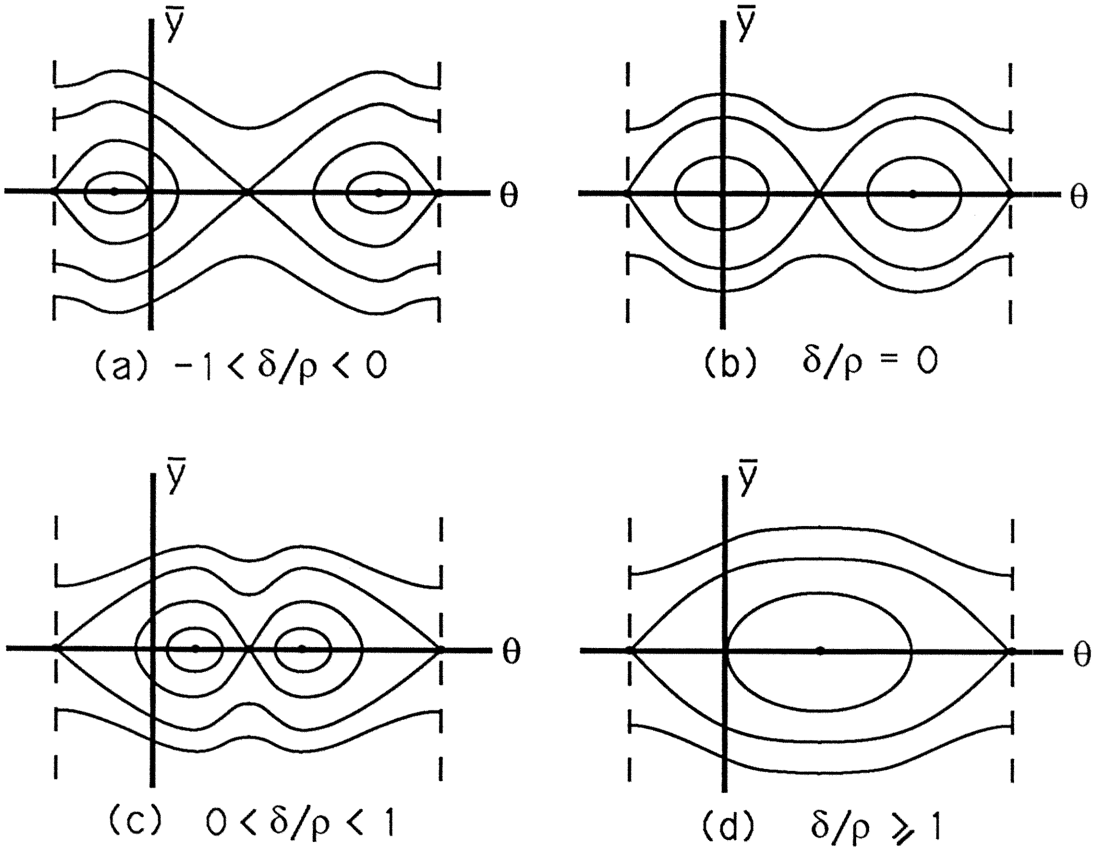

Figure 2.2 Qualitative structure of the phase portraits.

A second pair of fixed points satisfying $\sin\theta = \delta/\rho$ exists for $-1 < \delta/\rho < 1$. The two solutions for θ lying in $[-\pi/2, 3\pi/2)$ are $\theta = \sin^{-1}(\delta/\rho) \in (-\pi/2, \pi/2)$

and $\theta = \pi - \sin^{-1}(\delta/\rho) \in (\pi/2, 3\pi/2)$. The Hamiltonians and Jacobians are the same for both fixed points, specifically $H = -\rho^2(\frac{1}{2}\frac{\delta^2}{\rho^2} + \frac{1}{4})$ and $J = \rho^2(1 - \delta^2/\rho^2)$. Thus, since $-1 < \delta/\rho < 1$, both of these fixed points are centers whenever they exist. These two centers merge at $\theta = \pi/2$ when $\delta/\rho = 1$. The saddle at $\theta = \pi/2$ discussed above changes stability at this value of δ/ρ. So, at $\delta/\rho = 1$ a pitchfork bifurcation occurs with two centers collapsing onto a saddle, leaving only a center at $\theta = \pi/2$ for $\delta/\rho > 1$.

We illustrate the four qualitatively different phase portraits in Figure 2.2. A bifurcation involving separatrices occurs at $\delta/\rho = 0$ as described above. A pitchfork bifurcation occurs at $\delta/\rho = 1$. Since the topological structure of the orbits for $\delta/\rho = 1$ is the same as that of the orbits for $\delta/\rho > 1$, we show only one picture for the range $\delta/\rho \geq 1$

2.3.4 Physical interpretation of the orbits in the phase plane

In this subsection we give a physical interpretation of the results of the phase plane analysis in terms of the original dipole system shown in Figure 2.1. We illustrate the behavior of the dipole with schematic diagrams showing the physical motion of the dipole.

It is helpful to make a few observations about the relationship between various quantities in the planar system (2.7) and the original physical system. The distance between the two point vortices in the dipole is 2ρ and is constant in time. The point vortices stay a fixed distance apart and thus form a coherent dipole. Recall that $\bar{y}$ is the elevation of the center of the dipole above the horizontal axis and $\bar{x}$ is the distance the center of the dipole has moved along the horizontal axis from its initial position. The angle θ is the angle between the horizontal axis and the line drawn through the two point vortices. Since the dipole travels perpendicular to this line, a dipole oriented vertically (*i.e.*, $\theta = \pi/2$) will propagate horizontally. In what follows, we discuss each separate qualitative motion by noting the general behavior of $\bar{y}$ and θ from the phase plane analysis and indicating the behavior of $\bar{x}$ from (2.8) or (2.10).

The motions corresponding to the fixed points are the most important. These are uniform motions in which the elevation and inclination of the dipole are constant while the dipole propagates horizontally. The stability of the fixed points determines the stability of these uniform motions. The centers correspond to stable uniform motions while the saddles correspond to unstable ones. The unstable motions can be pushed into large-amplitude nonuniform motions by an arbitrarily small perturbation whereas the stable motions can only be induced to wobble a small amount by small perturbations. We will see below that dipoles in uniform motion to the left are unstable while those in uniform motion to the right are stable. Thus the model predicts that left moving modons will be unstable in the sense that their paths can be perturbed to finite-amplitude nonuniform paths by small perturbations. This surprising prediction is confirmed by simulations of modons in the next section.

We discuss the fixed points with $\cos\theta = 0$ first. At $\theta = -\pi/2$ the dipole is vertical with the point vortex with negative strength situated directly above the one with positive strength. The speed according to (2.8) is $-\rho(\rho+\delta)$ which is always negative. This fixed point is always a saddle, so this uniform motion to the left is always unstable. At $\theta = \pi/2$ the dipole is vertical with the positive point vortex situated above the negative one. The speed is $\rho(\delta-\rho)$. When $\delta < \rho$ the speed is negative and the fixed point is a saddle. When $\delta > \rho$ the speed is positive and the fixed point is a center. So this uniform motion is left-moving and unstable for $\delta < \rho$ and is right-moving and stable for $\delta > \rho$.

The fixed points with $\sin\theta = \delta/\rho$ are slightly different. Both fixed points are centers and both are stationary according to (2.8). So these fixed points correspond to stable stationary dipoles. The angle θ is not equal to $\pm\pi/2$, so these dipoles will be inclined skew to the vertical axis. Physically, the velocity induced by the point vortices on each other balances the velocity induced by the inclination of the dipole, so the dipole does not move.

The simplest nonuniform motions are those corresponding to orbits near the center at $\theta = \pi/2$ in Figure 2.2(d). These motions are small-amplitude periodic oscillations of $\bar{y}$ and θ. The dipole moves up and down while turning side to side slightly and propagating horizontally. The average speed is roughly that of the uniform motion corresponding to the fixed point at $\theta = \pi/2$. We refer to this motion as wobbling, illustrated schematically in Figure 2.3(a).

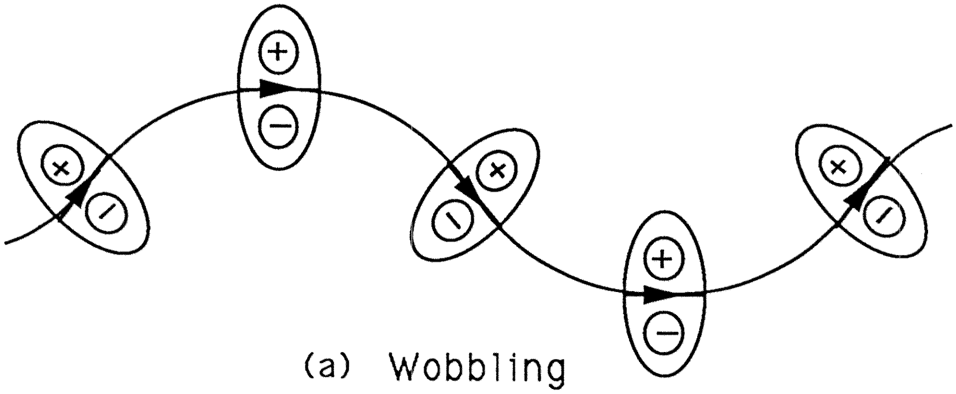

(a) Wobbling

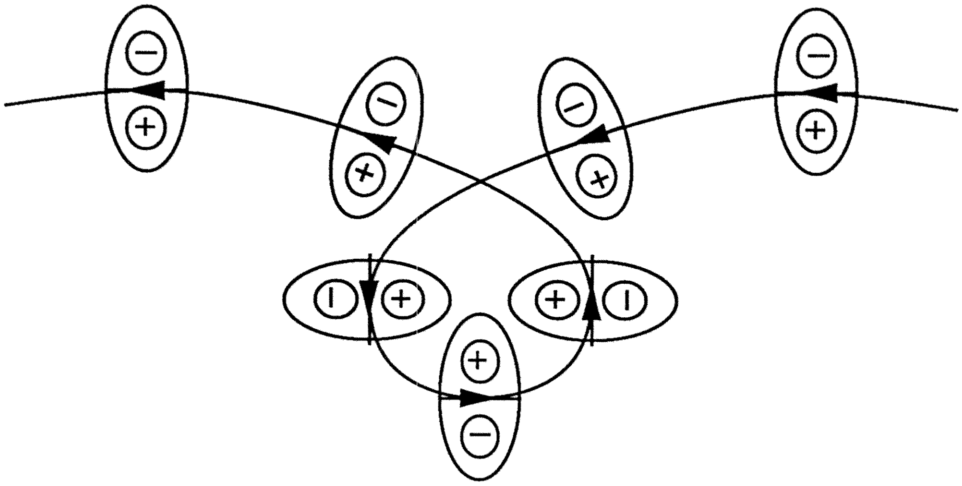

(b) Tumbling

Figure 2.3 Nonuniform motions exhibited by the dipole.

Figure 2.2(d) also contains periodic motions which are unbounded in θ. Examples of these orbits are those outside the eye–like separatrix. In these motions $\bar{y}$ oscillates about a finite value and θ increases or decreases monotonically without bound depending on the initial elevation and inclination. So, the dipole moves up and down while rolling in one direction. In general, the dipole will also propagate horizontally to the left since these orbits spend most of their time near the fixed point at $\theta = -\pi/2$. We refer to this motion as tumbling, shown schematically in Figure 2.3(b).

The various motions corresponding to the other orbits in Figure 2.2 are qualitatively similar to those described above. The examples we have described in detail serve to indicate the qualitative behaviors exhibited by the dipole.

2.4 Comparing Dipole Motions with Modon Motions

In this section we compare the results of the dipole model with those of actual modons in order to assess the success or failure of the model. We compare various properties of dipoles and modons in uniform motion in order to determine the parameter ranges in which the static properties of dipoles and modons agree. This leads to a specific choice of the parameters in the model for which the dipole will match the static properties of a given modon. We then go on to compare some nonuniform motions of a given modon with those of the appropriate dipole in order to assess the model's usefulness in predicting the complicated dynamical behavior of modons.

2.4.1 Properties of modons in uniform motion

In this subsection we discuss various properties of modons in uniform motion for the purpose of comparison with properties of the dipole model of the modon. We restrict our attention to the analytical solutions for modons given in Chapter 1, although other exact traveling wave solutions to the CHM equation may exist. We will discuss the qualitative nature of the modon's behavior, its dependence on parameters, and some quantitative attributes of the modon in terms of the parameters.

The modons described by the solution in Chapter 1 are all vertically oriented and propagate horizontally at constant speed, preserving their shape in a frame moving with the modon. A given modon is specified completely by its speed U and its radius a. Both U and a may be specified arbitrarily except that U must not lie in the interval $(-\beta/\gamma^2, 0)$.

The main quantitative attribute of a modon is the behavior of the associated streamfunction ψ far from the center of the modon. For $U > 0$ or $U < -\beta/\gamma^2$, the streamfunction for $r > a$ is given by

$$\psi_{modon} = -Ua\frac{K_1(pr/a)}{K_1(p)}\sin\theta \tag{2.11}$$

where $p^2 = a^2(\gamma^2 + \beta/U)$. For the stationary modon, $U = 0$ and $\psi \equiv 0$ for $r > a$. For the slowest left-moving modon, $U = -\beta/\gamma^2$ and $\psi = (\beta a/\gamma^2)\sin\theta$ for $r > a$.

The vertical gradient of ψ at the center of the modon is useful for measuring the near–field behavior. This is given by

$$G_{modon} = \frac{\partial\psi}{\partial r}(r = 0, \theta = \frac{\pi}{2}) = -U\left(1 + \frac{p^2}{q^2}(1 - \frac{1}{2J_1(q)})\right)$$

where q is the eigenvalue from the modon solution in Chapter 1. Other quantities, such as the total circulation or vorticity in each monopolar vortex of the modon, involve integrals of the streamfunction and are not useful for analytical comparisons.

2.4.2 Properties of dipoles in uniform motion

Here we present some properties of the dipole model presented in section 2.3 to compare with the properties of modons listed above. We first review the qualitative features of dipoles in uniform motion. We then list the quantitative properties of the dipole analogous to the properties for modons given in the previous subsection.

We saw in section 2.3 that the point vortex model yielded dipoles which could be specified by two arbitrary positive parameters, the strength κ_0 and the half-distance between point vortices ρ. The separation between the point vortices stayed constant in time so the vortices moved as a coherent dipolar structure. The uniform motions of these dipoles corresponded to fixed points of (2.7) and were motions in which dipoles of fixed size propagated horizontally at constant speed or were stationary. The dipoles corresponding to fixed points at $\theta = \pm\pi/2$ were oriented vertically. Those corresponding to fixed points with $\sin\theta = \delta/\rho$ were oriented skew to the vertical and were stationary. Below we list the quantitative properties of the dipoles for $\theta = \pm\pi/2$. We neglect the other dipoles since they are not vertically oriented whereas all the exact modon solutions are.

The motions corresponding to fixed points of (2.7) at $\theta = \pi/2$ moved at the constant speed $\rho(\delta-\rho)$ in the scaled time τ. The initial conditions for this fixed point require $y_0=\rho$, so the parameter δ must be given by $\delta=\kappa_0/\beta+\rho$. To obtain the actual speed of the dipole in the physical variables of (2.6) we must scale the speed by the factor $(\gamma\beta/\pi)K_1(2\gamma\rho)/2\rho$. We then find the actual speed of this dipole to be

$$U_{dipole}(\frac{\pi}{2})=\frac{\gamma\kappa_0}{2\pi}K_1(2\gamma\rho) \tag{2.12}$$

which is always positive. The streamfunction due to the two point vortices in the dipole can be computed using information in section 2.2. For this dipole, which has point vortices at $(0,\rho)$ and $(0,-\rho)$, the streamfunction far from the center of the dipole is

$$\psi_{dipole}(\frac{\pi}{2})\approx-\frac{\gamma\rho\kappa_0}{\pi}K_1(\gamma r)\sin\theta, \qquad r\gg\rho. \tag{2.13}$$

Similarly, the vertical gradient of ψ at the center of the dipole is

$$G_{dipole}(\frac{\pi}{2})=-\frac{\gamma\kappa_0}{\pi}K_1(\gamma\rho).$$

Similar expressions hold for the dipoles corresponding to fixed points of (2.7) at $\theta=-\pi/2$. The physical speed is given by

$$U_{dipole}(-\frac{\pi}{2})=-\frac{\gamma\kappa_0}{2\pi}K_1(2\gamma\rho)$$

which is always negative. The far-field behavior of the streamfunction is

$$\psi_{dipole}(-\frac{\pi}{2})\approx\frac{\gamma\rho\kappa_0}{\pi}K_1(\gamma r)\sin\theta, \qquad r\gg\rho.$$

The vertical gradient of ψ at the center of the dipole is

$$G_{dipole}(-\frac{\pi}{2}) = \frac{\gamma\kappa_0}{\pi}K_1(\gamma\rho).$$

2.4.3 Matching the dipole model to a given modon

In this subsection we compare the properties of modons in uniform motion to those of dipoles from the point vortex model. We first discuss the general qualitative comparisons between modons and dipoles. We then find the appropriate choices for the parameters κ_0 and ρ in order to match the speed and far–field behavior of a given modon. We give conditions on the speed and size of the given modon under which the parameters so chosen will yield a dipole which accurately models certain static properties of the modon.

Both modons and dipoles propagate as coherent dipolar structures. We have seen that modons can be found in uniform horizontal motion only oriented vertically. They can have arbitrary speed and radius, except that the speed must lie outside the interval $(-\beta/\gamma^2, 0)$. We found that dipoles could be found in uniform horizontal motion with some dipoles oriented vertically and others not. They can have arbitrary speed and size without any restriction. So, in general, we should expect that some dipole motions will qualitatively model modon motions while other motions exhibited by dipoles will not be found in modons.

In the previous subsection we saw that the dipole motions corresponding to fixed points of (2.7) at $\theta = \pi/2$ always moved with positive speed, while those for

$\theta = -\pi/2$ always moved with negative speed. We will compare the dipoles for $\theta = \pi/2$ to right–moving modons and compare those for $\theta = -\pi/2$ to left-moving modons.

Referring to (2.12), we see that we can match the speed of the right–moving dipoles to the speed U of a given right–moving modon by choosing the parameter κ_0 to be

$$\kappa_0 = \frac{2\pi U}{\gamma K_1(2\gamma\rho)}. \tag{2.14}$$

Using this value for κ_0 in the expression (2.13) for the far–field behavior of the dipole streamfunction, we find

$$\psi_{dipole}(\frac{\pi}{2}) \approx -2\rho U \frac{K_1(\gamma r)}{K_1(2\gamma\rho)} \sin\theta, \qquad r \gg \rho.$$

This will agree with the expression (2.11) for the modon streamfunction if we choose the parameter ρ to be

$$\rho = \frac{a}{2} \tag{2.15}$$

and provided that the parameter p in (2.11) is equal to $a\gamma$. Recall that p satisfies $p^2 = a^2(\gamma^2 + \beta/U)$, so $p \approx a\gamma$ provided $U \gg \beta/\gamma^2$.

The matching between left-moving dipoles and modons proceeds in much the same way. We find the same choices for κ_0 and ρ in terms of U and a. In this case, the far-fields agree provided $U \ll -\beta/\gamma^2$. So the dipole can be tuned to match the speed and far-field behavior of a given modon provided $\mid U \mid \gg \beta/\gamma^2$. We note here that the quantity β/γ^2 is the phase velocity for waves of infinite wavelength of the linearized CHM equation.

It is also instructive to compare the near–field behavior of the dipole with that of the modon. We do this by comparing the gradient of the streamfunction at the center, G, for each. Recall that for the modon this is given by

$$G_{modon} = -U\left(1 + \frac{p^2}{q^2}(1 - \frac{1}{2J_1(q)})\right).$$

For the dipole, with parameters chosen to match the modon as above, this is

$$G_{dipole} = -U\frac{2K_1(\gamma a/2)}{K_1(\gamma a)}.$$

In general, these are of the same sign and magnitude. For small a, it can be shown that $G_{modon} \rightarrow -U$ and $G_{dipole} \rightarrow -4U$. Note, however, that for large a with fixed U we have

$$G_{modon} \rightarrow -U\frac{\gamma^2}{\tilde{q}^2}\left(1 - \frac{1}{2J_1(\tilde{q})}\right)a^2,$$

while

$$G_{dipole} \rightarrow -2\sqrt{a}Ue^{\gamma a/2},$$

where $\tilde{q} \approx 5.1356$ is the asymptotic value of the eigenvalue q as $a \rightarrow \infty$ (see Chapter 1). Thus the gradients are comparable for moderate values of a but are of different orders of magnitude when a is large.

To summarize, we have found that some of the uniform motions found in the dipole model compare well with uniform modon motions. The parameters in the model can be chosen so that the speed and far-field behavior of the dipole match those of a given modon, provided the speed of the modon is large compared with the phase speed for waves of infinite wavelength for the linearized CHM equation. We have also seen that the near-field properties of the dipole are in qualitative agreement with those of the modon provided the radius of the modon is not large. The near-field properties are never in good quantitative agreement, however. Thus, we expect qualitative agreement between the nonuniform motions of a given modon and those of the appropriately chosen dipole provided that the modon is relatively small and fast.

2.4.4 Comparison of nonuniform motions of dipoles and modons

In this subsection we compare various nonuniform motions of modons with those of the appropriately chosen dipoles. The results quoted for modons are from direct numerical simulations of the CHM equation with initial conditions corresponding to various initial states of the modon. The results for the model dipoles are either analytical or are known very accurately from the solution of the system of ordinary differential equations in (2.6) or (2.7).

The numerical method used to simulate the CHM equation closely follows those found elsewhere (*e.g.,* Makino, Kamimura, and Sato [1981] and Makino, Kamimura, and Taniuti [1981]). In brief, each hyperbolic step in updating the quantity $\kappa = \nabla^2\psi - \gamma^2\psi$ is performed according to a standard optimized alternating direction method (Gourlay and Morris [1970]). The solution of the elliptic problem $\nabla^2\psi - \gamma^2\psi = \kappa(x,y)$ once κ is known is obtained using a standard Fast Fourier Transform package. To retain spatial accuracy and consistency, the finite difference derivatives in the hyperbolic step are evaluated to fourth order in space with periodic boundary conditions. We use a square spatial grid of length 10 on each side with 256 grid points in each direction with time steps ranging from $\Delta t = 0.001$ to $\Delta t = 0.0004$.

In all cases, we have taken $\gamma = \beta = 1$ in the CHM equation. Since the exact modon solution is known only for modons in uniform horizontal motion, we simulate the nonuniform motions by using the exact modon solution tilted at some angle α initially. Figure 2.4 shows this configuration schematically. This is analogous to taking initial data with $\bar{y} = 0$ and $\theta = \pi/2 + \alpha$ in the model equations (2.6) or (2.7). We demonstrate that the resulting motions of the tilted modon are nearly periodic and agree qualitatively with those of the model dipole.

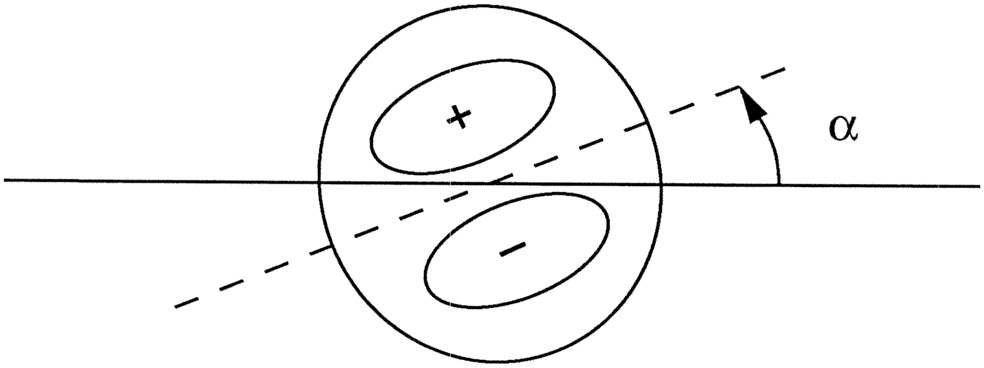

Figure 2.4 Geometry of the wobbling modon.

A complete study of the motion of a modon tilted initially at $\alpha = 0.3$ illustrates the wobbling behavior of the modon. Figure 2.5 shows physically the position and

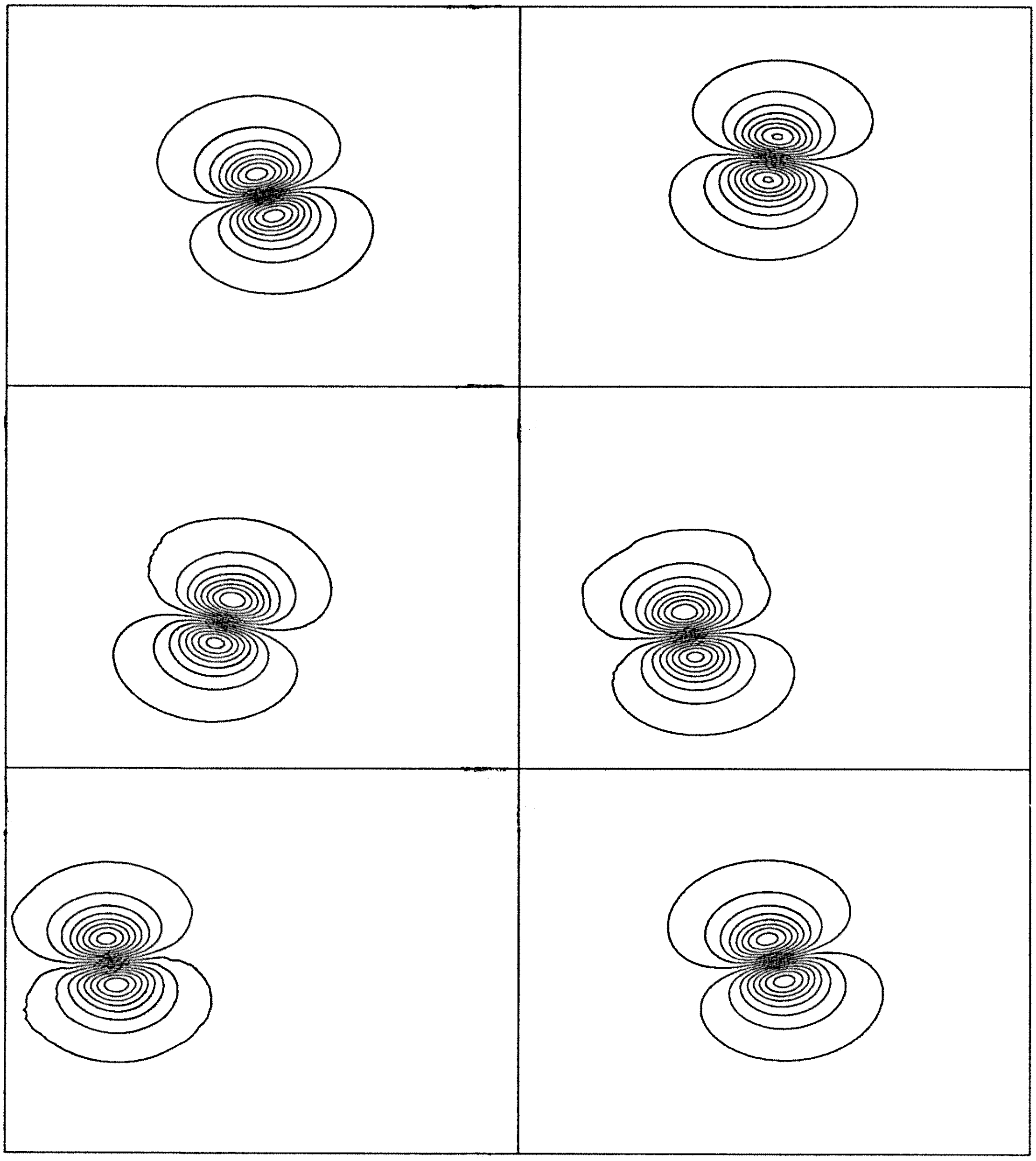

Figure 2.5 Physical behavior of a tilted modon, $\alpha = 0.3$.

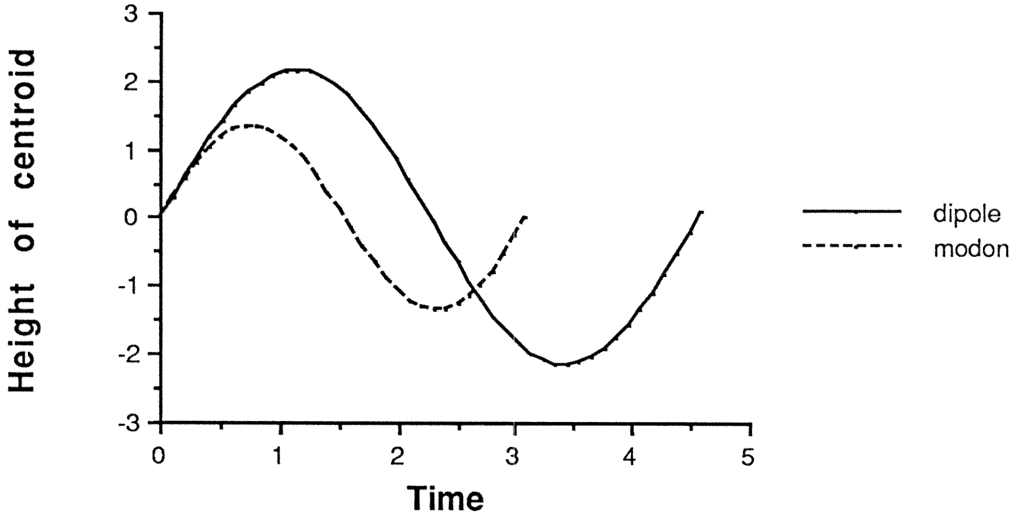

Figure 2.6 Height of the centroid of modon and dipole vs. time.

shape of the modon at various times in the course of one period of motion. We have used a right-moving modon with speed $U = 10$ and radius $a = 1$. The modon rises and drops vertically while twisting back and forth. The shape and distribution of vorticity remain nearly constant during the motion, justifying the assumption that the motion is coherent. The juxtaposition of the modon initially and at the end of the period in the bottom two frames shows that it returns to very nearly its original shape and distribution. Figure 2.6 shows plots of the height of the centroid, $\bar{y}$, versus time for the modon and for the dipole with parameters chosen to match. The period and amplitude of the wobbling is greater for the dipole than for the modon, but the two are qualitatively the same. Here and elsewhere we have taken the parameters in the dipole model to correspond to the speed and far-field behavior of the modon according to equations (2.14) and (2.15). The appropriate half-separation between the point vortices is $\rho = 0.5$ while the appropriate vortex strength is $\kappa_0 = 104.388$.

The wobbling behavior of the modon can be studied as a function of the initial angle α. We have plotted the period of motion for the modon and the dipole versus α in Figure 2.7 (a). Similarly, the average horizontal speed over the period of motion for each is plotted in Figure 2.7 (b). The period and average speed of the modon are obtained by observing the position of the centroid over time. The dipole period and average speed are given in equations (2.18) and (2.19) in the appendix to Chapter 2. As expected, the qualitative agreeement between the dipole and the modon is quite good in both plots. The speed of the model dipole agrees very well quantitatively with that of the modon, deviating only for large-amplitude motions.

The stable wobbling behavior of a right-moving modon about its uniform state is contrasted by the unstable behavior of a slightly perturbed left-moving modon. This was predicted by the model and can be shown directly by simulating a perturbed left-moving modon numerically. We have performed two simulations of a modon with speed $U = -10$ and radius $a = 1$ strated with the centroid at height $\bar{y} = 5.0$. The first modon was tilted initially at an angle $\alpha = 0.01$, while the second was tilted initially at $\alpha = 0.1$. These correspond to two slightly perturbed left-moving modons. Figure 2.8 is a plot of the height of the centroid for each case versus time. Obviously the deviation of the centroid from its equilibrium height is of much larger order than the perturbation parameter α. In both cases, the centroid

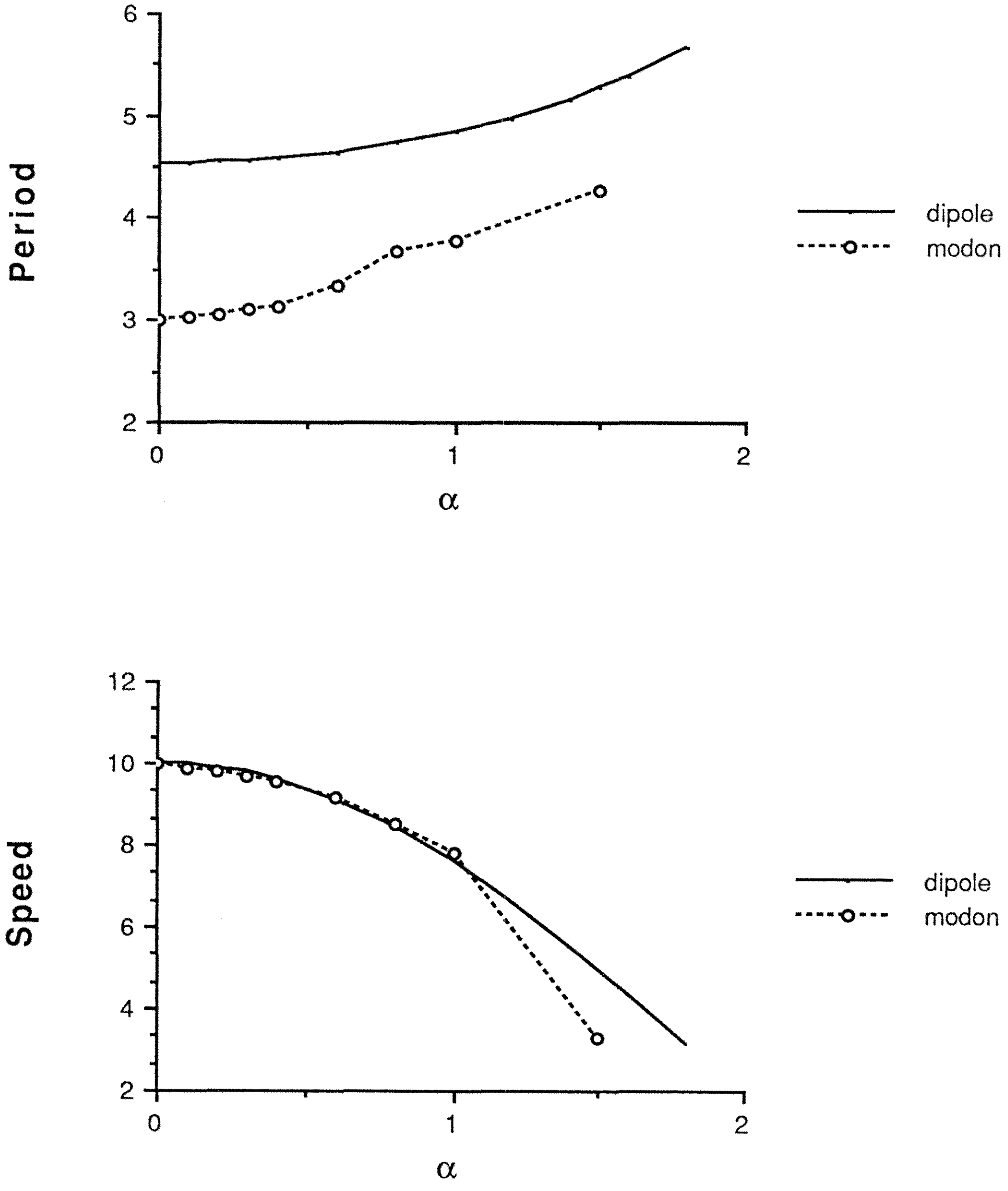

Figure 2.7 Period and average speed of modon and dipole vs. α.

initially diverges from its equilibrium $\bar{y} = 5.0$ exponentially in time. For $\alpha = 0.1$, we see the modon exhibits a highly nonuniform motion. We conclude that the path of a left-moving modon in uniform motion is unstable and is perturbed to a finite-amplitude state regardless of the size of α. Previous numerical studies with which we are familiar have not simulated perturbed left-moving modons.

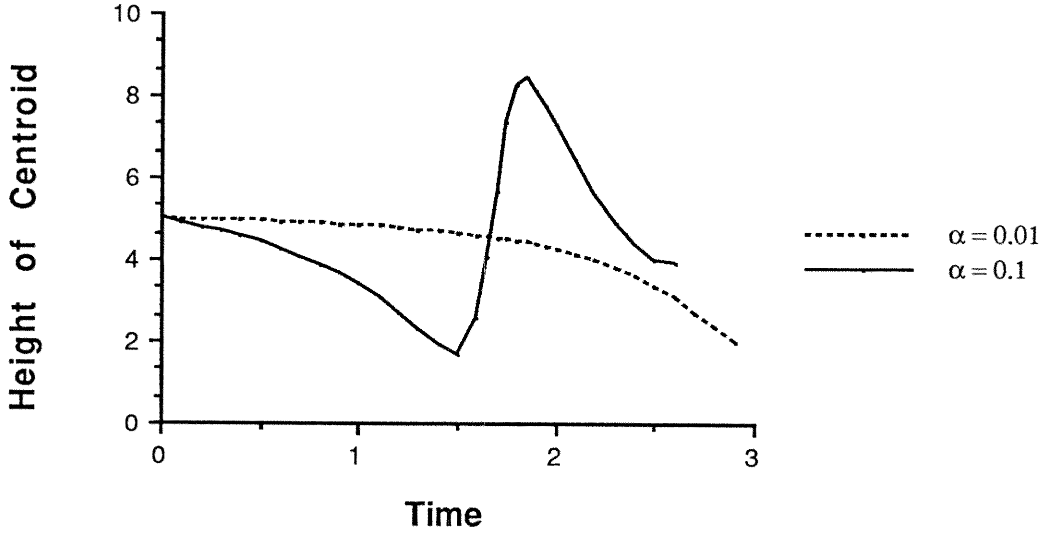

Figure 2.8 Height of the centroid of a perturbed left-moving modon vs. time.

We note that this result alters the previous understanding of modon stability. Based on previous analysis and numerical simulations, modons appear to be stable in the sense that they retain their strongly isolated dipolar structure even when strongly perturbed. Based on the present analytical model and numerical simulation, however, their paths can depend very sensitively on their initial orientation. This note should be appended to the work of Laedke and Spatschek [1985] and Sakuma and Ghil [1990] who showed respectively that the vorticity distributions of the left-moving and stationary modons are stable in the Lyapunov sense.

2.5 Conclusions

In this chapter we have applied a point vortex model to study the motions of a single isolated modon. We found all the possible motions exhibited by a model dipole. Some of these motions are well-known, such as the uniform horizontal and wobbling motions, while others have not been observed before, such as the tilted stationary states and large-amplitude tumbling motions. We also found that the model predicted that right-moving modons would be stable and left-moving modons would be unstable in the sense of their paths being perturbed by small perturbations in their initial positions and inclinations.

We showed that the model could be used to match the speed and far-field behavior of a given modon in uniform motion by an appropriate choice of model parameters provided that the modon was sufficiently small and fast. Using specific parameter values, we compared the behavior of a model dipole with the behavior of a modon placed in nonuniform motion by direct numerical simulation of the modon. We found the period and average speed of wobbling motions of the dipole to be in good agreement with those of the modon for small and moderate amplitude wobbling. We also confirmed the model prediction that the left-moving modon in uniform motion can be perturbed into a large-amplitude nonuniform motion by arbitrarily small perturbation in its initial inclination. We noted that it is important to consider this path stability in addition to the stability of the vorticity distribution considered by others.

Appendix: Solution of Planar System in Terms of Elliptic Functions

In this appendix we show how the planar system (2.7) can be solved in terms of elliptic functions. We reduce the system to a first-order equation and give a general expression for its solution. We evaluate this expression explicitly for the case $\delta/\rho > 1$ to illustrate the solution technique and to obtain an expression for the period of oscillation and average speed for the wobbling dipole.

Recall the planar system (2.7) is given by

$$\frac{d\bar{y}}{d\tau} = -\rho\cos\theta(\delta - \rho\sin\theta)$$

$$\frac{d\theta}{d\tau} = -\bar{y}.$$

The system is 2π–periodic in θ. It is symmetric about $\theta = \pi/2$ and $\bar{y} = 0$. So, it is sufficient to study the region of the phase plane given by $-\pi/2 \le \theta \le \pi/2$ and $\bar{y} \le 0$. This corresponds to the lower left quarter of the phase plane diagrams in Figure 2.2.

This choice of bounds on θ and $\bar{y}$ makes the following obvious reductions convenient. Define the new variables

$$\tau' = \rho\tau \qquad\qquad u(\tau') = \sin\theta(\tau)$$

and define the parameter

$$\mu = \frac{\delta}{\rho}.$$

The $(\bar{y}, u)$ system can then be reduced to a single second-order equation for u. This equation can be integrated once to get the following equation for u:

$$\left(\frac{du}{d\tau'}\right)^2 = \left(A - (u-\mu)^2\right)(1-u^2) \tag{2.16}$$

where A is a constant of integration. The bounds on θ and $\bar{y}$ ensure that the transformation between u and θ is one–to–one and that the derivative of u will always be the positive root of (2.16). The parameter μ must satisfy $\mu > -1$.

The equation for u is of the form

$$\left(\frac{du}{d\tau'}\right)^2 = (a-u)(b-u)(c-u)(d-u)$$

where the roots a, b, c, and d are constant and satisfy $a > b > c > d$. This equation can be solved very simply in the case that the roots are distinct. The solution for $c \leq u \leq b$ parametrized so that $u(0) = c$ is

$$u(\tau') = \frac{c - dD\mathrm{sn}^2(\tau'/g, k)}{1 - D\mathrm{sn}^2(\tau'/g, k)} \tag{2.17}$$

where

$$k^2 = \frac{(b-c)(a-d)}{(a-c)(b-d)}, \qquad g = \frac{2}{\sqrt{(a-c)(b-d)}}, \qquad D = \frac{(b-c)}{(b-d)}$$

and $\mathrm{sn}(x, k)$ is a Jacobian elliptic function (Byrd and Friedman [1954]). In the cases where the roots are not distinct, the solution can be obtained either as a limit of the generic solution above or by solving (2.16) directly.

We now evaluate the solution (2.17) explicitly for $\mu > 1$ to obtain an expression for the orbits corresponding to the wobbling motion of the dipole about a stable uniform motion. The initial conditions $u(0) = u_0$, $u'(0) = 0$ correspond to the leftmost extreme of one of the orbits in Figure 2.3.2 (d) surrounding the center at $\theta = \pi/2$. Then $A = \Delta^2$ where $\Delta = \mu - u_0$. The value $\Delta = \mu - 1$ corresponds to the center itself and values for which $\mu - 1 < \Delta < \mu + 1$ correspond to the orbits surrounding the center. The roots are $a = \mu + \Delta$, $b = 1$, $c = \mu - \Delta$, $d = -1$. The solution is

$$u(\tau') = \frac{\mu - \Delta + \frac{1}{2}(1 + \Delta - \mu)\mathrm{sn}^2(\sqrt{\Delta}\tau', k)}{1 - \frac{1}{2}(1 + \Delta - \mu)\mathrm{sn}^2(\sqrt{\Delta}\tau', k)}$$

where $k^2 = ((1 + \Delta)^2 - \mu^2)/4\Delta$.

It is easy to show that the period of these wobbling motions is just the period of $\mathrm{sn}(\sqrt{\Delta}\tau', k)$. The period in τ' is then $4K(k)/\sqrt{\Delta}$ where $K(k)$ is the complete elliptic integral of the first kind. To find the physical period of the wobbling recall that the physical time t is related to the scaled time τ by $\tau = (\gamma\beta/\pi)(K_1(2\gamma\rho)/2\rho)t$ and $\tau' = \rho\tau$. The physical period T is then

$$T = \frac{\pi}{\gamma\beta}\frac{2\rho}{K_1(2\gamma\rho)}\frac{4K(k)}{\rho\sqrt{\Delta}}. \tag{2.18}$$

The average speed c' of the dipole in the scaled variables of (2.7) can be obtained from (2.10). After multiplying this by the factor $(\gamma\beta/\pi)K_1(2\gamma\rho)/2\rho$ to obtain the average speed c in the physical variables of (2.6), we find

$$c = \frac{\gamma\beta}{\pi}\frac{K_1(2\gamma\rho)}{2\rho}\frac{\rho^2}{K(k)}\int_0^{K(k)} (\mu - u(s))u(s)ds. \tag{2.19}$$

For the motion of the right-moving dipole tilted initially off axis at an angle α, the quantity Δ can be expressed in terms of α as $\Delta = \mu - \cos\alpha$.

CHAPTER 3

Fluid Flow and Mixing in the Dipole Model

3.1 Introduction

In this chapter we use the point vortex dipole model developed in Chapter 2 to study the flow of fluid around an isolated modon. This has relevance in the study of modons as atmospheric blocks. It has been assumed that a modon in the atmosphere completely shields its interior from the external flow. We establish that this is not the case for modons in nonuniform motion, where significant mixing may occur even for small amplitude nonuniform motions. This may also provide a mechanism for enhanced energy transport in tokamak plasmas even when the particle transport is not great.

We first give the equations for the particle paths around a model dipole. We note that when the dipole wobbles the resulting system of ordinary differential equations for the particle paths can be reduced to a planar map by use of the Poincare map. We discuss a mechanism for chaotic mixing in such maps and show that the system for particle paths around a wobbling dipole exhibits such mixing. We plot invariant manifolds for the dipole, roughly equivalent to the distribution of a carefully placed blob of tracer dye after evolving for some time in the flow. This illustrates the amount of mixing as a function of the wobbling amplitude.

3.2 Equations for Particle Paths

In this section we give the equations governing the motion of fluid particles in the flow field due to a dipole. We first give the general equations in physical variables for the motion of fluid particles due to an arbitrary distribution of point vortices. We then specialize the equations to the dipole case.

Fluid particles move with the velocity induced by the streamfunction. For a distribution of n point vortices the streamfunction is the sum of the streamfunctions ψ_n for the individual point vortices, given by equation (2.2) in Chapter 2. The fluid velocity $\mathbf{v} = (\dot{x}, \dot{y})$, using expressions (2.3) and (2.5), is then

$$\frac{dx}{dt} = -\frac{\partial}{\partial y}\left(\sum_n \psi_n\right) = -\frac{\beta\gamma}{2\pi}\sum_n \frac{K_1(\gamma|\mathbf{x}-\mathbf{x}_n|)}{(|\mathbf{x}-\mathbf{x}_n|)}(\kappa_n^0/\beta + y_n^0 - y_n)(y - y_n)$$

$$\frac{dy}{dt} = \frac{\partial}{\partial x}\left(\sum_n \psi_n\right) = \frac{\beta\gamma}{2\pi}\sum_n \frac{K_1(\gamma|\mathbf{x}-\mathbf{x}_n|)}{(|\mathbf{x}-\mathbf{x}_n|)}(\kappa_n^0/\beta + y_n^0 - y_n)(x - x_n)$$

where $\mathbf{x}_n = (x_n(t), y_n(t))$ is the position of the n^{th} point vortex at time t.

We can simplify this expression in the case that the point vortex distribution is that of the dipole described in Chapter 2. In that case the initial strengths and positions of the vortices are

$$\kappa_1^0 = -\kappa_2^0 = \kappa_0 \qquad x_1^0 = -x_2^0 = -x_0 \qquad y_1^0 = -y_2^0 = y_0$$

We again define the parameters δ and ρ by

$$\delta = \frac{\kappa_0}{\beta} + y_0 \qquad\qquad \rho^2 = x_0^2 + y_0^2$$

and rescale time as follows:

$$\tau = \frac{\beta\gamma}{2\pi}\frac{K_1(2\gamma\rho)}{\rho}t.$$

The equations for fluid motion around the dipole in a frame moving with the average speed of the dipole are

$$\frac{dx}{d\tau} = \frac{-\rho}{K_1(2\gamma\rho)}\left(\frac{K_1(\gamma r_1)}{r_1}(\delta - y_1)(y - y_1) - \frac{K_1(\gamma r_2)}{r_2}(\delta + y_2)(y - y_2)\right) - c'$$

$$\frac{dy}{d\tau} = \frac{\rho}{K_1(2\gamma\rho)}\left(\frac{K_1(\gamma r_1)}{r_1}(\delta - y_1)(x - x_1) - \frac{K_1(\gamma r_2)}{r_2}(\delta + y_2)(x - x_2)\right). \tag{3.1}$$

where $r_i = |\mathbf{x} - \mathbf{x}_i|$ and c' is the average speed using the scaled time τ. For a dipole in uniform motion with $x_0 = 0$ and $y_0 = \rho$, the particles paths follow the streamlines in a frame moving with the dipole, shown in Figure 3.1. Note that the stagnation points are located at $(\pm\sqrt{3}\rho, 0)$ and the top of the streamline separating the external flow from the flow inside the dipole is at a height proportional to ρ. So the region of fluid trapped in the dipole has roughly the same area and shape as that of the modon, which traps a circular region of fluid with radius $a = 2\rho$.

The point vortex positions $(x_1(t), y_1(t))$ and $(x_2(t), y_2(t))$ are expressible in terms of the elliptic function solution given in the appendix to Chapter 2. This solution is useful in that it gives the average speed of the vortices and the period of their oscillation. For simulating the particle paths numerically it is more efficient to solve the primitive equations for the vortex paths in parallel with the particle path equations. These equations, given in (2.6) in Chapter 2, coupled with equations

(3.1) above constitute a complete set of equations for simulating the particle paths around a dipole.

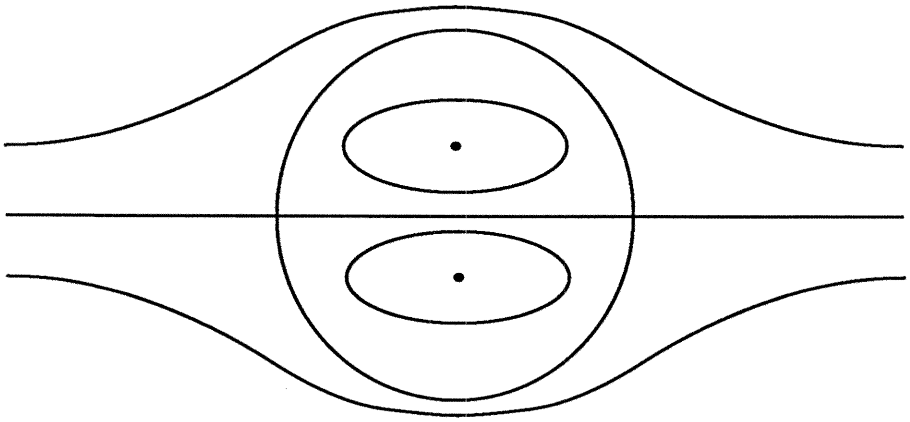

Figure 3.1 Streamlines past a dipole in uniform motion.

3.3 General Structure of Poincare Maps

In this section we study the general structure of Poincare maps of periodic flows. This is motivated by the fact that the flow of particles given by (3.1) is in general periodic in time. The reduction of the equations to a map will greatly simplify the study of transport and mixing in the fluid. Before we can apply the Poincare map we must study the nature of the type of map we expect and relate various structures to their analogs in the original flow.

The Poincare map is the map of points in the plane to their positions one period later, after moving with velocity given by (3.1). To be precise, let the period be T. The image of the point (x_0, y_0) under the Poincare map starting at time t_0 is the solution $(x(t_0+T), y(t_0+T))$ of (3.1) with initial condition $(x(t_0), y(t_0)) = (x_0, y_0)$. Formally this can be written

$$P_{t_0} : \begin{pmatrix} x(t_0) \\ y(t_0) \end{pmatrix} \rightarrow \begin{pmatrix} x(t_0+T) \\ y(t_0+T) \end{pmatrix}$$

where P_{t_0} is the Poincare map. Thus a time–periodic flow can be reduced to a planar map simply by taking snapshots of the flow at discrete times differing by one period of the flow.

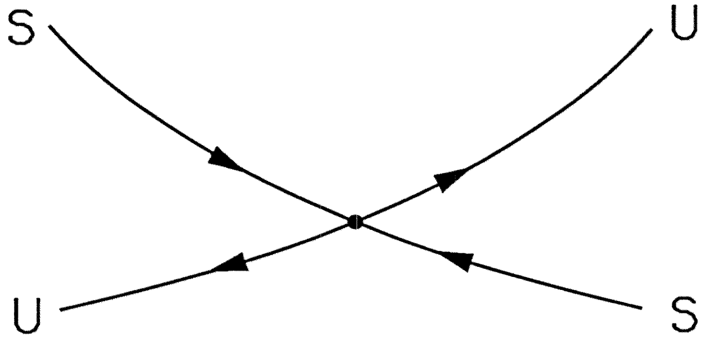

Figure 3.2 Local structure of manifolds.

It is useful to relate some of the structures in the map to their counterparts in the original flow. Fixed points of the map will correspond to periodic orbits in the flow with the same period as the flow field itself. Locally, fixed points of planar maps are similar to those of planar ordinary differential equations. Hyperbolic fixed points of planar maps will have stable and unstable manifolds as shown in Figure 3.2. The stable manifold of a hyperbolic fixed point is the set of points whose forward images under the map asymptote to the fixed point. The unstable manifold is the set of points whose backward iterates asymptote to the fixed point. These sets form smooth connected curves in the plane. Although individual points on the manifolds are mapped to other points when the map is applied, the curves themselves do not change. Thus they are called invariant manifolds.

These manifolds are equivalent to streaklines in the original flow. A blob of tracer dye placed in the flow enclosing the fixed point will contract towards the fixed point along the stable manifold and stretch away from the fixed point along the unstable manifold. In time the ink will stretch further and further, tracing out the shape of the unstable manifold. So the unstable manifold actually attracts fluid locally, even though the name might suggest otherwise.

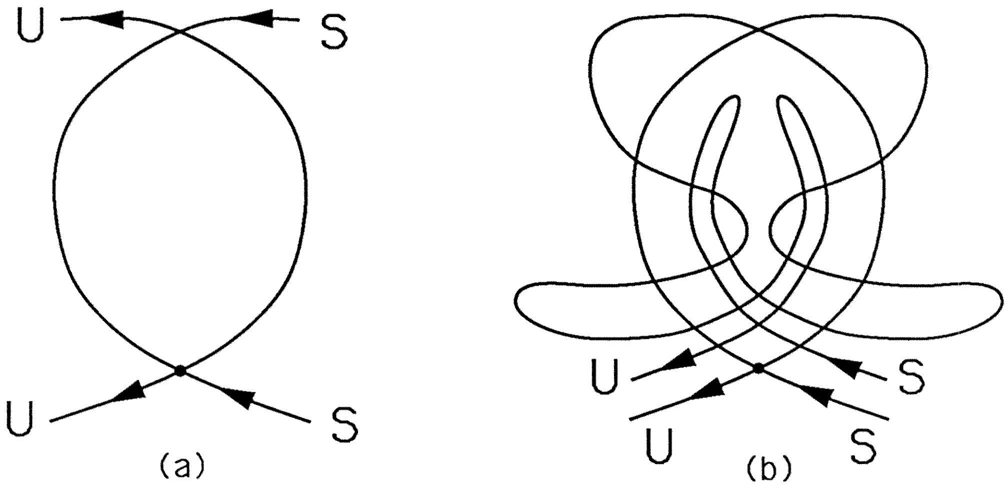

Figure 3.3 Global structure of manifolds.

The global structure of these manifolds may be quite different from manifolds of fixed points in planar ordinary differential equations. The stable and unstable manifolds of a fixed point of the map may intersect transversely, as shown in Figure 3.3 (a). The point of intersection lies on both the stable and unstable manifolds, denoted by S and U for convenience. Note that all forward and backward images of any point in S are also in S, and likewise for U. Thus all forward and backward images of the intersection must lie in both S and U, and thus must also be intersection points. So S and U must intersect at an infinite number of points which asymptote forward or backward to the fixed point, as indicated in Figure 3.3 (b).

For incompressible flows, such as the flow around the dipole, a simple closed curve will evolve in such a way that the enclosed region contains the same fluid particles and has constant area. This property is inherited by the Poincare map of such a flow. A given region will be mapped to a second region so that the boundary of the first region is mapped to the boundary of the second region and the area of the first is equal to the area of the second. This simple observation can be used to explain the mechanism of transport in the map.

Figure 3.4 illustrates the transport mechanism in maps in which the stable and unstable manifolds of a fixed point intersect. We call regions O_1, O_2, etc... outer lobes because they lie outside the main body of the α–shaped structure. Regions I_1, I_2, etc... are called inner lobes because they lie inside. The fluid in region O_1 is mapped in a 1–1 fashion to O_2, and region O_2 is mapped to region O_3. Region O_3 then passes into the main body as it is mapped to I_4. Region I_4 is then mapped to I_5 and then to I_6 and so on. Thus, fluid from the outer lobes is mapped to the inside lobes. This fluid may be trapped forever or may escape to the outside again. This is the case for the fluid in the portion of region I_6 which intersects with region O_4. This fluid will pass to O_5, then O_6 and so on. Similarly, fluid initially inside the main body can escape to the outside. This provides a simple mechanism for mixing between the fluid inside the main body and the external flow.

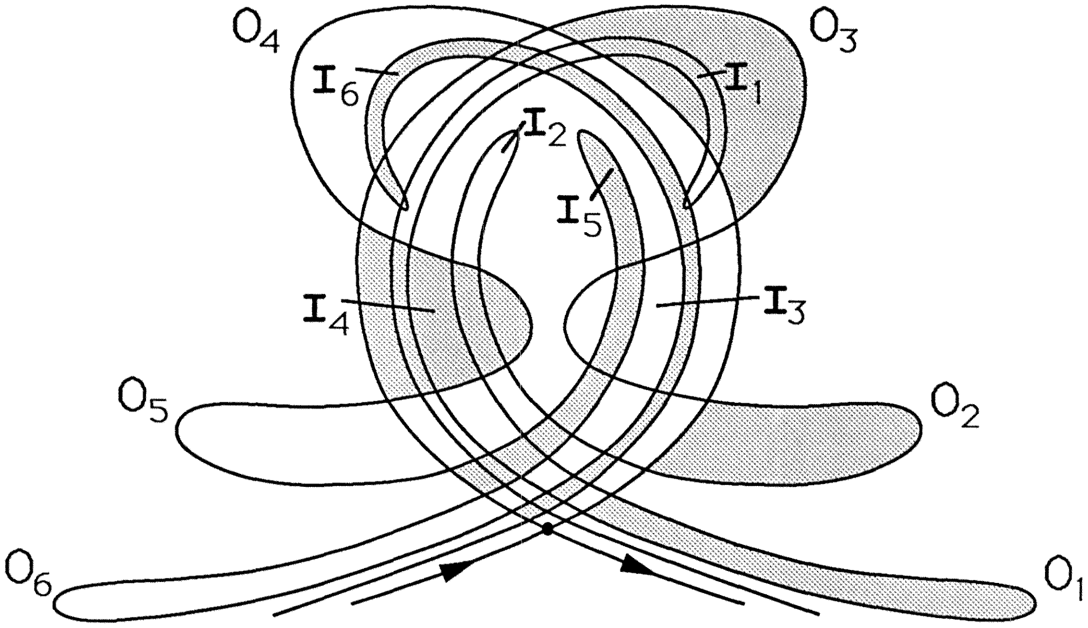

Figure 3.4 Transport mechanism in maps with tangling manifolds.

This mixing is actually chaotic in the sense that the position of a fluid particle after N iterates of the map is a very sensitive function of its initial position. The tangling near the fixed point is responsible for this chaos. Two particles near the fixed point and close together initially can be split apart and carried off by different parts of the flow so that their separation after only a few iterations is quite large. This chaos can be established rigorously by showing that some iterate of the map acts as a horseshoe map on some region of the flow. A more detailed treatment of a similar problem appears in Rom-Kedar, Leonard, and Wiggins [1990].

3.4 Structure of the Poincare Map for Particle Flow

In this section we study the structure of the Poincare map for the particle flow around a dipole. We apply the ideas developed in the previous section to establish that the manifold in the map tangle with each other when the dipole wobbles. We demonstrate this numerically by plotting short segments of the manifolds to show that they intersect. We note the technique for establishing this analytically and relegate the details to an appendix.

We consider the flow of particles around dipoles in periodic motion. For simplicity, consider the wobbling motions corresponding to the periodic orbits surrounding the stable fixed point in Figure 2.2 (d). The equations (3.1) for the particle paths are then time-periodic and can be reduced to a planar map by using the Poincare map. We choose the initial time t_0 for the map so that the dipole is oriented vertically with its center on or above the horizontal axis. For uniform motion the center lies on the axis while for wobbling the center will start above the axis, with larger amplitude wobbling for the center farther above the axis initially. We take the period T of the map to be the period of motion of the point vortices, given by the expression (2.18) in the appendix to Chapter 2. We also use a reference frame traveling horizontally with the average speed of the point vortices, given by equation (2.19) in the same appendix.

The structure of the Poincare map for the dipole in uniform motion is identical to the graph of the streamlines for the dipole in Figure 3.1. This is so because streamlines and streaklines are the same in autonomous flows. This flow has no natural period, since it is autonomous, so we take the limit of the period for the wobbling motion as the amplitude of wobbling approaches zero. The map has two fixed points, corresponding to the two stagnation points of the dipole flow. The unstable manifold of the right fixed point coincides with the stable manifold of the left fixed point. Likewise, one branch of the stable manifold of the right fixed point coincides with one branch of the unstable manifold of the left fixed point. This corresponds to the fact that the leading and trailing stagnation points of the dipole flow are connected by separatrices which are streamlines. Note that in this case the external flow is barred from the inside of the dipole by the streamlines connecting the stagnation points.

The local structure of the Poincare map persists when the dipole wobbles. The fixed points of the map remain and retain their stability type for sufficiently small amplitude wobbling. These correspond to two small amplitude periodic orbits in the dipole flow close to the original two stagnation points, with the same period as the wobbling motion. These fixed points retain their stable and unstable manifolds with the same orientation locally. These manifolds correspond to one-parameter families of orbits in the dipole flow which asymptote to one of the periodic orbits in either forward or backward time.

The global structure is quite different, however, as shown in Figure 3.5. The separatrices in the uniform flow are broken in the nonuniform flow. The upper and lower branches of the unstable manifold of the right fixed point no longer coincide with their counterparts of the stable manifold of the left fixed point. Instead, these manifolds tangle with one another in the fashion described in section 3.3. Likewise, one branch of the stable manifold of the right fixed point tangles with one branch of the unstable manifold of the left fixed point.

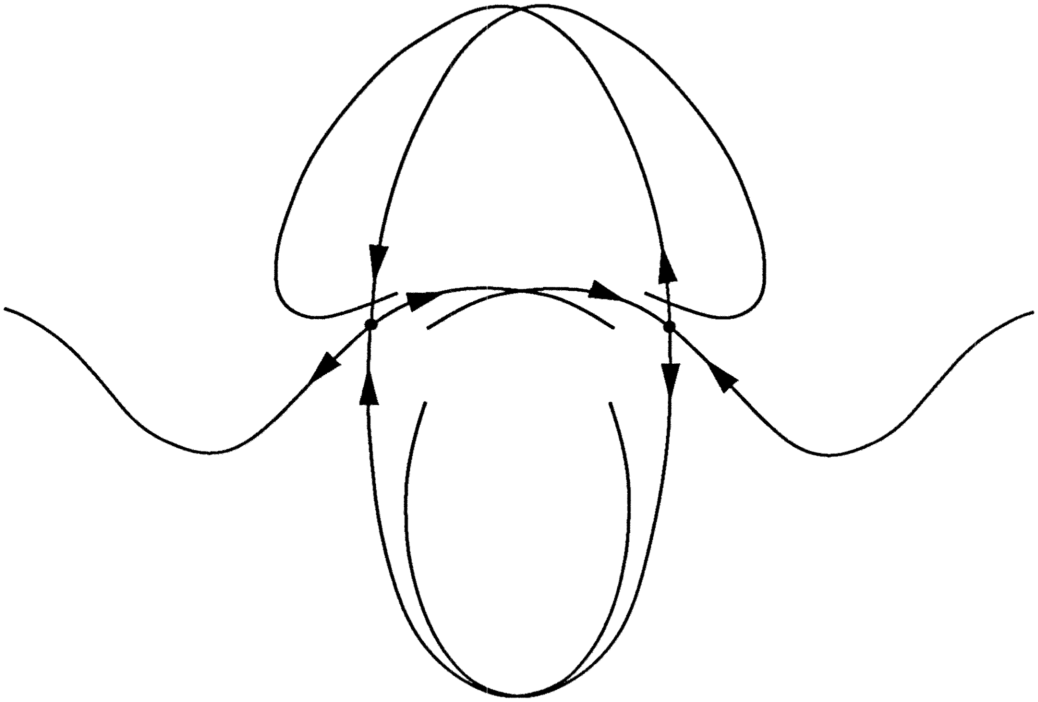

Figure 3.5 Structure of manifolds for a perturbed dipole.

The plots of manifolds in Figure 3.5 establish numerically that the tangling described in Section 3.3 occurs in the particle flow around the wobbling dipole. As we saw in Section 3.3, this is simply a consequence of the fact that the manifolds cross transversely at some point. We can also establish this fact analytically for small amplitude wobbling by computing the so-called Melnikov function for each pair of manifolds which intersect with each other. This function is an estimate of the perpendicular distance between two manifolds close to one another as a function of a parameter which parametrizes the parallel distance along the manifolds. We give the details of this calculation in Appendix 1 at the end of this chapter and show that it implies that the manifolds for the wobbling dipole tangle with one another in the limit of small wobbling.

Having established that the manifolds of the Poincare map of the dipole flow tangle, we can infer that the particle paths around the wobbling dipole are in general chaotic functions of their initial positions. Thus a passive marker particle placed in the flow of a wobbling dipole will move chaotically. We would expect that if a third point vortex were placed in the flow its motion would be still more sensitive to its initial position, owing to its unpredictable effect on the two point vortices making up the dipole. Hence, we would expect that the motion of three point vortices in this model will be chaotic in general. This contrasts the point vortices for the Euler equations which exhibit chaotic motion only for groups of four or more point vortices (Aref and Pomphrey [1982]).

3.5 Mixing Between the Dipole and the External Flow

In this section we study the mixing between the fluid inside the dipole and the fluid in the external flow. For the dipole in uniform motion, no mixing occurs because the two flows are separated by the streamlines connecting the stagnation points of the dipole flow, as shown in Figure 3.1. When the dipole wobbles, however, mixing occurs due to the tangling of the manifolds of the Poincare map for the dipole flow. We study this phenomenon in more detail below and show plots of the manifolds to see how the amount of mixing depends on the wobbling amplitude.

We showed in the previous section that the manifolds of the Poincare map for the dipole flow tangle. As described in Section 3.3, this leads to mixing between the fluid inside the dipole and the external flow. Although this mixing is chaotic, we can estimate the amount of fluid involved in the mixing by getting estimates of the area enclosed between tangling manifolds. This is very difficult to do analytically, but by plotting the manifolds in various cases we can get an idea of how the mixing zone behaves as a function of the wobbling amplitude.

Figure 3.6 contains plots of the stable and unstable manifolds generated numerically for four different wobbling amplitudes. A brief description of the method used to compute these manifolds appears in Appendix 2 at the end of this chapter. Each plot represents the qualitative structure of the flow for a specific wobbling amplitude.

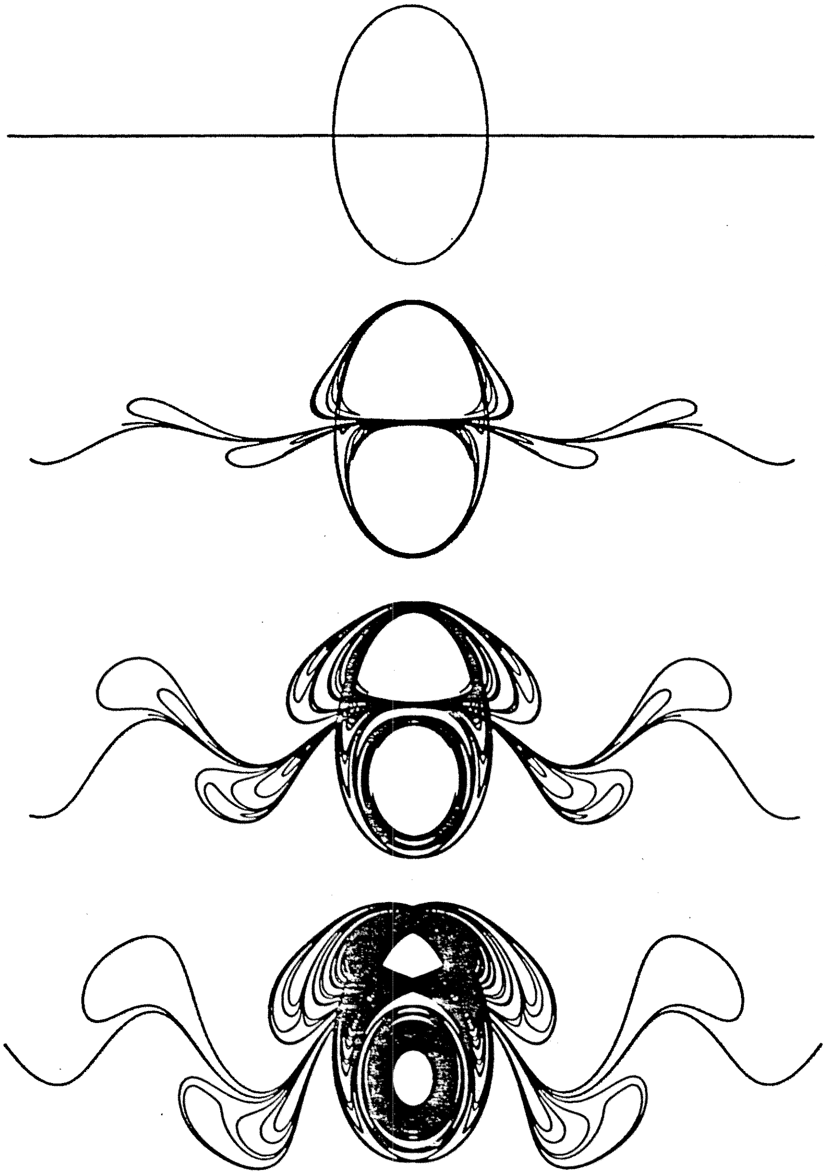

Figure 3.6 Manifolds of the wobbling dipole for various α.

As noted in Section 3.3, these manifolds are streaklines in the flow, viewed once per period of wobbling. These manifold plots resemble the flow after blobs of ink placed around the two fixed points have evolved over many periods. The region of the flow in which mixing occurs is indicated by this ink. Thus these plots give a pictoral idea of the size of the mixing zone for each wobbling amplitude.

Figure 3.6 (a) is a plot of the streamlines around the dipole in uniform motion. No mixing between the dipole and the external flow occurs in this case. Figure 3.6 (b) is a plot of the tangling manifolds for a wobbling amplitude of $\alpha = 0.1$. This amplitude α is defined as the maximum angle of inclination to the horizontal axis of the dipole as it wobbles. The manifolds tangle in a thin layer near the separatrices found in the uniform flow. There is a core region inside each half of the dipole which is not affected by the tangling. Thus fluid neither escapes from nor enters these core regions. Similarly, the external flow is only affected by the tangling near the outside of the dipole and the sparse lobes along the horizontal axis. Thus the mixing zone, the region affected by the tangling, is rather small in this case.

Figures 3.6 (c) and (d) show how the mixing zone grows as the amplitude increases. For $\alpha = 0.3$, the mixing zone has increased dramatically in size from that for $\alpha = 0.1$, occupying roughly half the area inside the dipole. For $\alpha = 0.5$, the mixing zone occupies almost the entire area of the dipole. For slightly larger α the core regions will disappear completely and all the fluid inside the dipole will mix with the external flow.

The mixing of fluid between the dipole and the external flow is an obvious mechanism of transport for passive quantities. Active quantities, such as heat, can be passed diffusively across interfaces between two fluids. An initially smooth region of fluid in the shape of the unperturbed dipole will in general deform so that its surface looks more and more like the unstable manifolds. The interface between the fluid inside the dipole initially and the external flow will stretch dramatically in time. Several theories exist which predict that this length stretching is exponential in time, and we have confirmed this numerically using accurate plots of the unstable manifolds. Thus, the potential for greatly enhanced diffusion between the fluid inside the dipole and the external flow exists due to the exponential stretching of the interface between the two fluids.

So, in general nonuniform motions, we would expect that significant mixing occurs between the dipole and the external flow. For uniform horizontal motion no mixing occurs. But, even for small amplitude wobbling motions the fluid inside the dipole which does not mix is only a fraction of the total fluid in the dipole. For large amplitude wobbling and for the tumbling motions described in Chapter 2, we would expect that almost all the fluid in the dipole mixes with the external flow.

The implications for modons are rather obvious, based on the assumption that the flow around modons in nonuniform motion is qualitatively the same as the flow around dipoles. A significant amount of the fluid inside the modon can mix with the external flow. This undermines the assumption that modons transport all the fluid initially inside them and divert the external flow completely around them. Thus modons may not serve as complete atmospheric blocks in general. This fluid mixing should also be significant for modons in tokamak plasmas, where collisions and highly nonuniform motion would presumably prevail in a fluid containing many modons. Also, the surface stretching would provide a mechanism for energy transport in such plasmas. It has been assumed that the modons trap energy in the fluid. But thermal energy may be transported rapidly even if the energy in the fluid motions is not.

3.6 Conclusions

In this chapter we have shown that mixing between the fluid inside a model dipole and the external flow occurs whenever the dipole is not in uniform horizontal motion. We described the general mechanism of chaotic mixing or Lagrangian turbulence in related flows and showed that the wobbling dipole exhibited such mixing by studying stable and unstable manifolds (streaklines) in a Poincare map of the flow. We showed that the manifolds intersect and tangle analytically, by computing a Melnikov function, and numerically, by plotting the manifolds. We used plots of very long manifolds to graphically estimate the amount of mixing which occurs as a function of the wobbling amplitude.

The physical implications of this mixing are based on the assumption that the particle paths around a dipole are qualitative the same as those around a modon. Given that, it is clear that relatively small deviations from straight horizontal motion can cause significant mixing between the modon and the external flow. In atmospheric flows, the rate of this mixing is likely to be slow compared with the lifetime of the modon. So, modons should serve as good, though not complete, atmospheric blocks. In tokamak plasmas, it is impossible to know how important this mixing is since there have been no observations of modons in tokamaks. We can only say that this mixing may provide a mechanism for enhanced energy diffusion through the plasma without enhanced particle diffusion.

Appendix 1: The Melnikov Function

In this appendix we give a brief outline of the Melnikov function based on the derivation in the book by Guckenheimer and Holmes [1983]. The Melnikov function is a measure of the transverse distance between stable and unstable manifolds of Poincare maps and is useful in establishing analytically that the manifolds tangle in the limit of small-amplitude perturbation.

Consider a planar system of ordinary differential equations in the form

$$\dot{\mathbf{x}} = \mathbf{f}(\mathbf{x}) + \epsilon \mathbf{g}(\mathbf{x}, t)$$

where $\mathbf{g}$ is periodic in time with period T. Suppose that for $\epsilon = 0$ the system has phase portraits as in Figure 3.7 (a). We denote the separatrix by $\mathbf{x}^0(t)$, with $\mathbf{x}^0(\pm\infty) = \mathbf{p}^0$. Note that one branch of each the stable and unstable manifolds of the fixed point $\mathbf{p}^0$ coincide to form this separatrix.

For the perturbed problem, with $\epsilon \neq 0$, we study the Poincare map for the system which maps each point in the plane to its position after evolving under the flow for one period. If, for example, $\mathbf{g}(\mathbf{x}, t) = \sin\omega(t + t_0)$ and we take the Poincare sections at times $t = 0$, T, $2T$, $3T$, ... then t_0 is the phase of the forcing $\mathbf{g}$ relative to the Poincare sections. For ϵ sufficiently small, this map has a fixed point $\mathbf{p}^\epsilon$ which is ϵ-close to $\mathbf{p}^0$. This fixed point has stable and unstable manifolds S and U which are ϵ-close to the unperturbed separatrix along the portions which are close to the fixed point p^ϵ, as shown in Figure 3.7 (b).

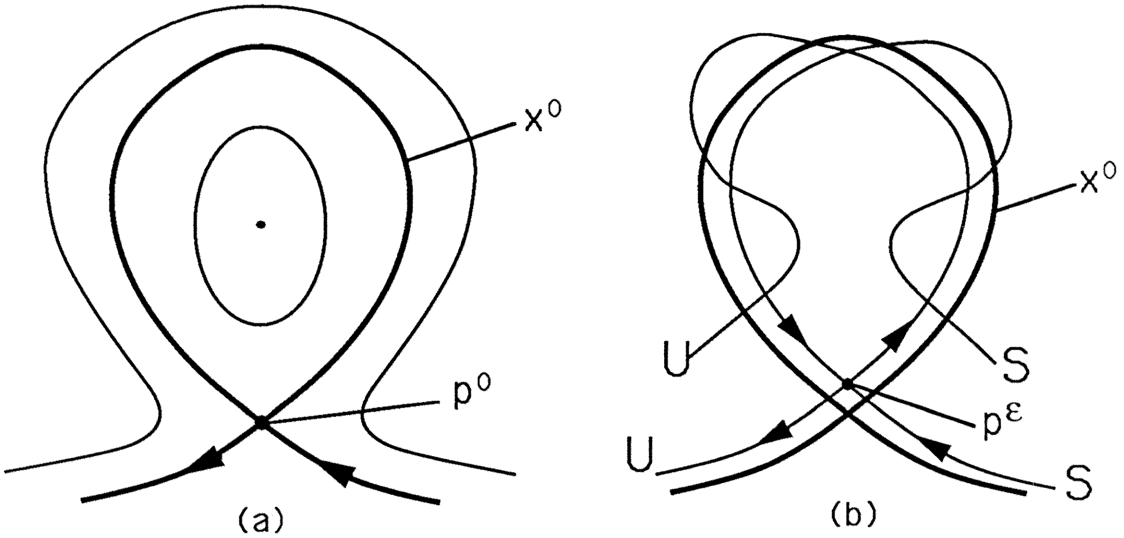

Figure 3.7 Structure of the unperturbed and perturbed systems.

The Melnikov function is a measure of the distance between S and U which requires knowledge only of the unperturbed separatrix, $\mathbf{x}^0(t)$. Figure 3.8 shows the geometry for the calculation. The separation between S and U measured along a line perpendicular to $\mathbf{x}^0(t)$ at a point $\mathbf{x}^0(0)$ along the unperturbed separatrix is

$$d(t_0) = \frac{\epsilon M(t_0)}{|\mathbf{f}(\mathbf{x}^0(0))|} + O(\epsilon^2)$$

where the Melnikov function, in a form useful for calculations, is given by

$$M(t_0) = \int_{-\infty}^{\infty} \mathbf{f}(\mathbf{x}^0(t)) \times \mathbf{g}(\mathbf{x}^0(t), t + t_0) dt.$$

Since $\mathbf{f}(\mathbf{x}^0(0)) \neq 0$, $M(t_0)$ serves as a good measure of the distance between the manifolds perpendicular to the unperturbed separatrix. It can be shown, for sufficiently small ϵ, that if $M(t_0)$ has a simple zero then S and U must cross transversely. This single crossing would imply an infinite number of crossings, as discussed in Section 3.3, and hence the tangling of S and U. If $M(t_0)$ has no zeroes, then the manifolds do not cross.

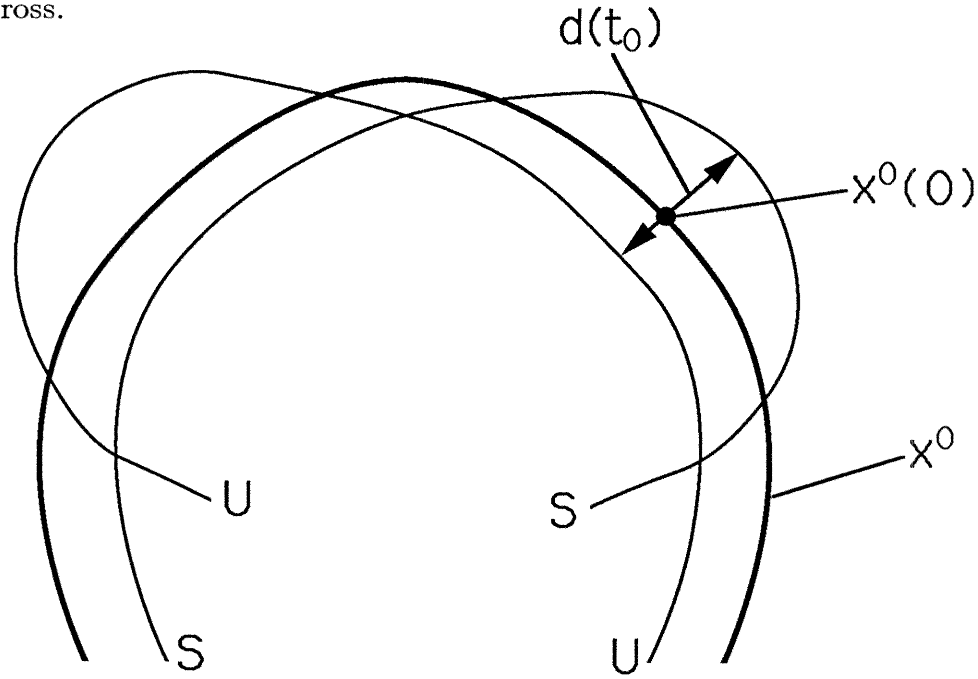

Figure 3.8 Geometry for the calculation of the Melnikov Function.

The equations for fluid motion around a slightly wobbling dipole admit an analogous Melnikov function measuring the distance between perturbed manifolds. The position of fluid particles, in a reference frame moving with the average speed of the dipole, evolves according to the Hamiltonian

$$H = \frac{1}{\gamma K_1(2\gamma\rho)}\Big((\delta + y_2)K_0(\gamma r_2) - (\delta - y_1)K_0(\gamma r_1)\Big) + c'y$$

where r_1 and r_2 are the distances from the point vortices in the dipole, located at $\mathbf{x}_1$ and $\mathbf{x}_2$ respectively, and c' is the average speed of the dipole using the scaled time τ. To repeat the Melnikov analysis for this system, it is necessary to expand H in ϵ, a small parameter representing the amplitude of wobbling of the dipole. Thus we write $H = H_0 + \epsilon H_1 + O(\epsilon^2)$ where H_0 is the time-independent Hamiltonian of the unperturbed system and

$$H_1(\mathbf{x}, t) = \left(\frac{\partial H}{\partial \epsilon}\right)_{\epsilon=0}.$$

In this Hamiltonian formulation the Melnikov integral is found to take the form [Guckenheimer and Holmes]

$$M(t_0) = \int_{-\infty}^{\infty} \{H_0, H_1\}_{(x(t), y(t), t+t_0)} dt$$

where $\{U, V\} = U_x V_y - V_x U_y$ is evaluated in its spatial entries on the unperturbed separatrix, given by $(x(t), y(t))$, and in its temporal entry at the shifted time $t + t_0$.

We can evaluate the Melnikov function in this case using the limiting forms of the elliptic function solutions found in the appendix to Chapter 2. Making use of some symmetries in the resulting integrals, we find

$$M(t_0) = I_1 \cos(\rho t_0 \sqrt{\mu - 1})$$

where I_1 is independent of t_0. The value of I_1 depends only on the parameters in the problem and the particular unperturbed separatrix on which it it evaluated. As shown in Figure 3.1, the unperturbed dipole has three separatrices, each of which may break and tangle under the wobbling perturbation. Thus the Melnikov function has simple zeroes on each separatrix provided that I_1 is nonzero along each separatrix.

The expression for I_1 is given by

$$I_1 = 2\Lambda \int_0^\infty \Big(\{D, A\} \sin(\rho t \sqrt{\mu - 1}) + \{D, B\} \cos(\rho t \sqrt{\mu - 1}) \Big) dt$$

where the functions $A(x, y)$, $B(x, y)$, and $D(x, y)$ are evaluated along each of the the unperturbed separatrices separately and $\{D, A\} = D_x A_y - A_x D_y$. The constant Λ is given by

$$\Lambda = \sqrt{2(\mu - 1)}\rho \left(\frac{\rho(\delta - \rho)}{\gamma K_1(2\gamma\rho)} \right)^2$$

and the functions A, B, and D are given by

$$A = \sqrt{\mu - 1} \left(\frac{1}{\delta - \rho} \Big(K_0(\gamma r_2) + K_0(\gamma r_1) \Big) + \gamma^2 \Big((y + \rho) \frac{K_1(\gamma r_2)}{\gamma r_2} - (y - \rho) \frac{K_1(\gamma r_1)}{\gamma r_1} \Big) \right)$$

$$B = \gamma^2 \left(\frac{K_1(\gamma r_2)}{\gamma r_2} + \frac{K_1(\gamma r_1)}{\gamma r_1} \right) x$$

$$D = K_0(\gamma r_2) - K_0(\gamma r_1) + \gamma K_1(2\gamma\rho) y$$

where $r_1 = \sqrt{x^2 + (y - \rho)^2}$ and $r_2 = \sqrt{x^2 + (y + \rho)^2}$. We have found numerically that I_1 is different from 0 on each of the three separatrices for all values of the parameters tested, except for the case $\delta = \rho$. In this case the system for the paths of the point vortices themselves is singular, so it is not surprising that this analysis breaks down there. Physically this is the case where the two point vortices have zero initial strength, the so-called 'ghost' vortices [Zabusky and McWilliams]. Thus we have shown that for sufficiently small wobbling amplitude all three separatrices of the dipole break and tangle in the fashion described in Section 3.3.

Appendix 2: Computation of Invariant Manifolds

In this appendix we outline our method for generating the stable and unstable manifolds for Poincare maps. The method we describe is applicable to all planar maps that have such manifolds. We give the general mathematical principle on which the computations are based and describe some of the details of the numerical implementation.

The general problem is to compute stable and unstable manifolds which emanate from a hyperbolic fixed point of a planar map. The location of the fixed point and the local structure of these manifolds is assumed to be known from analysis or highly accurate numerics. It is convenient to work with segments of the manifolds which are smooth curves with one endpoint being the image under the map of the other endpoint. Suppose that such a segment on the unstable manifold close to the fixed point is known. The next segment along the unstable manifold is then the image of this initial segment. This image segment by construction will join smoothly with the initial segment, its first point being the last point of the initial segment. This process can be repeated recursively to produce an arbitrary number of segments joined end to end along the unstable manifold. This is shown schematically in Figure 3.9. An initial segment denoted by 1 is mapped to segment 2, which is mapped to segment 3 and so on. The same process can be repeated for the inverse of the map to generate the stable manifolds.

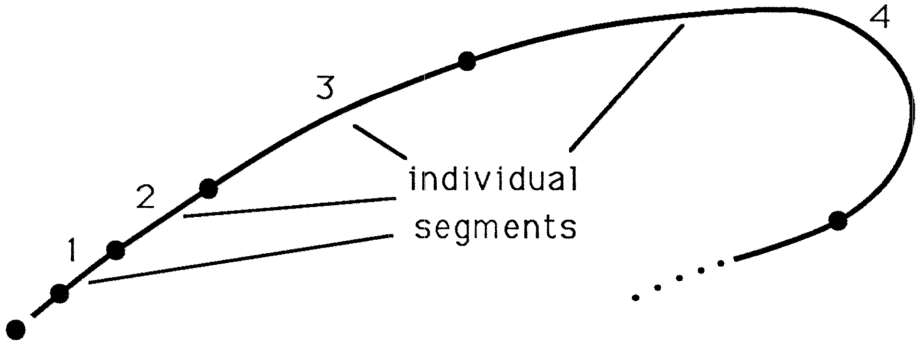

Figure 3.9 Successive segments compose a portion of the manifold.

Of course, it is not possible to map all the points in a given segment forward to obtain the next segment. It is practical, however, to use a finite approximation to the segment to generate a finite approximation to the next segment. Our finite approximation to a segment consists of a set of points $\{(x_i, y_i, s_i)\}_{i=0}^{i=N}$ which specifies cartesian coordinates x and y and arclength s at points along the segment. These points are chosen so that the segment is resolved uniformly throughout its length with a minimum number of points. Using this data, we can interpolate a point $(\bar{x}, \bar{y})$ on the segment corresponding to a given arclength $\bar{s}$. This is shown in Figure 3.10. To generate the next segment, we start with $\bar{s} = s_0$ and increase $\bar{s}$ incrementally until $\bar{s} \geq s_N$. Along the way, we interpolate the point $(\bar{x}, \bar{y})$ for each $\bar{s}$ and map it forward to find an image point in the next segment. The problem is to determine the appropriate increments in $\bar{s}$ so that the image points will resolve the next segment without using too many points.

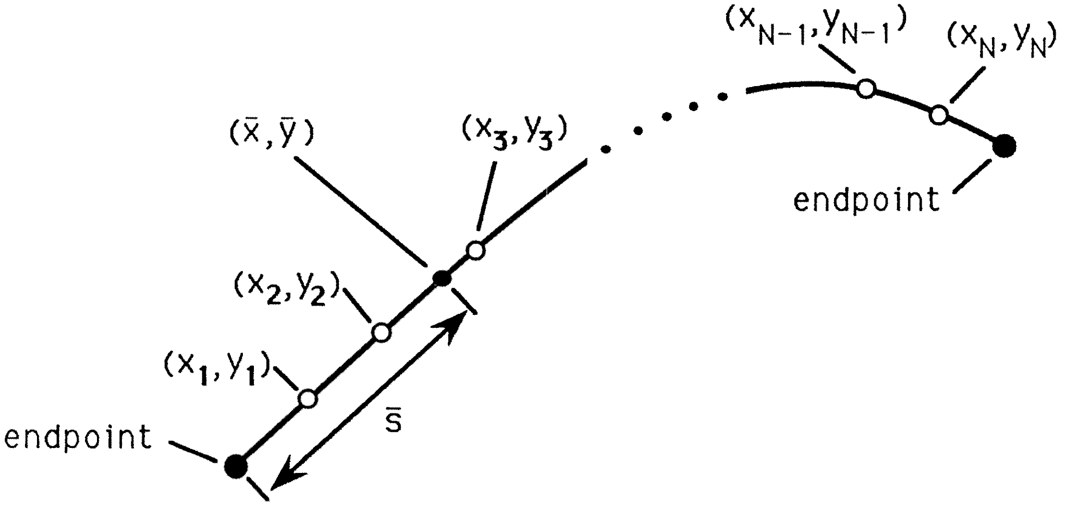

Figure 3.10 Interpolation of a pre-image between known points.

We determine the increments in $\bar{s}$ by monitoring each newly generated image point. We require that the angle formed between three successive image points be smaller than a given tolerance (typically between 0.1 and 0.5). This method is illustrated in Figure 3.11. We suppose that we have some image points on the new segment already and have a starting value for the increment in $\bar{s}$, namely ds. We find the point on the known segment corresponding to the arclength $\bar{s}+ds$ and map it forward to find a trial image point. We calculate the angle between this point and the two previous points in the new segment. If this angle is too large we decrease ds and start again. This process is repeated until the angle is sufficiently small or until ds drops below some minimum stepsize. In the latter case the image point is saved and we proceed to the next point, noting that a violation of the resolution criterion occurred. If the angle is sufficiently small the image point is saved and we proceed, leaving ds unchanged. If the angle is smaller than a minimum angle, we save the image and increase ds. The first few points on the new segment needed to get this method started are obtained either by generating images using the minimum stepsize or by monitoring the angle between the image points and points at the end of the initial segment.

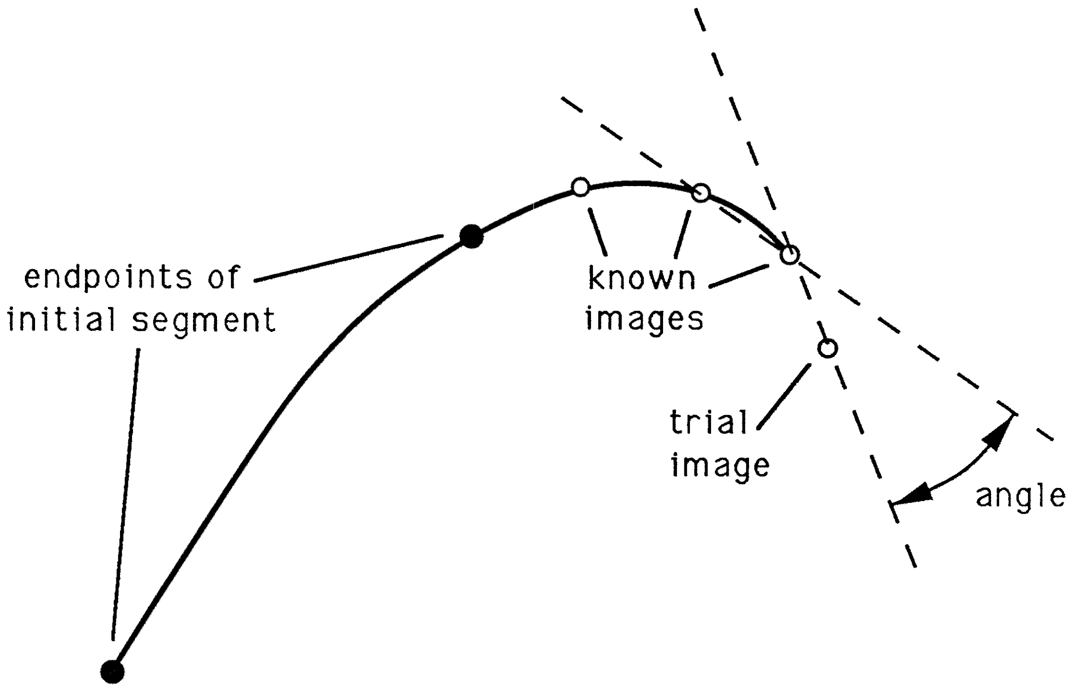

Figure 3.11 Angle formed by three successive image points.

Monitoring the angle between points has roughly the same effect as monitoring the spacing between points relative to the local radius of curvature. Formulas for curvature can give poor results when the points are far apart or spaced nonuniformly. The angle, however, is a well-behaved quantity so we have chosen to monitor it instead. The resulting manifolds are smoothly resolved throughout their length with a minimum number of points, *i.e.,* a minimum number of calls to the map itself. This is especially important for Poincare maps of continuous systems, where evaluating the map involves integrating a differential equation for one period.

CHAPTER 4

Coaxial Collisions of Dipoles

4.1 Introduction

Collisions between modons will occur in any fluid which contains many modons, such as might be the case for a tokamak plasma (Jovanovic [1988]). It is thus important to understand collisions between two modons. Numerical simulations of modon collisions reveal some of the possible behavior, as shown in Figure 4.1. A systematic study of collisions by direct simulation is impractical, however. In this

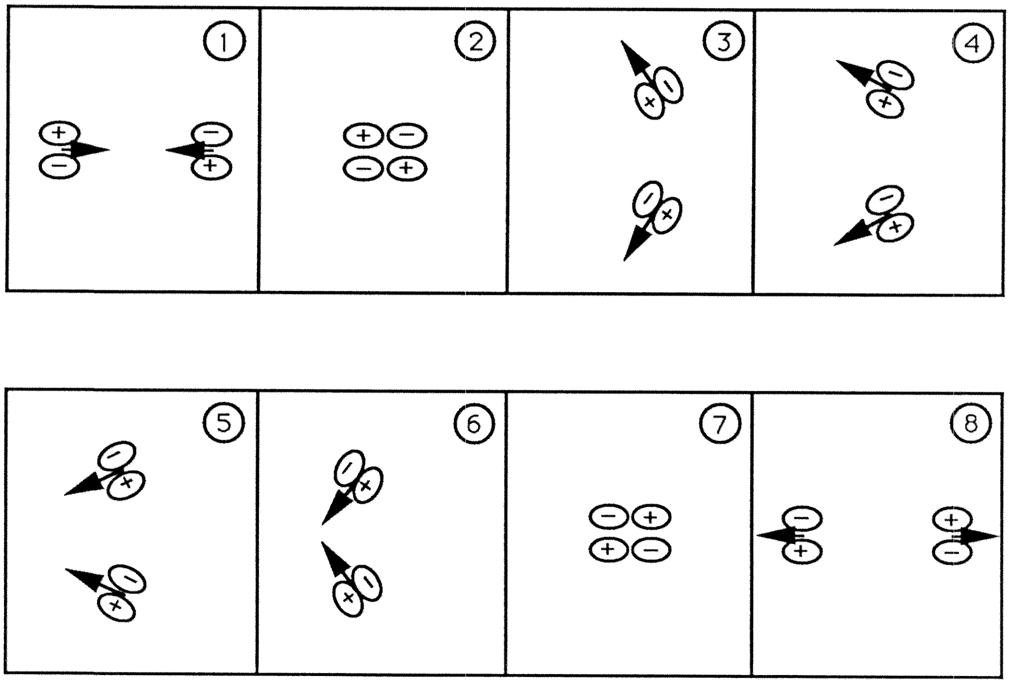

Figure 4.1 A schematic example of a collision between two modons.

chapter we study the coaxial collision of two modons using the point vortex dipole model of Chapter 2 in order to perform a systematic study analytically. We hope that a complete understanding of these simple collisions will indicate the behaviors expected in general collisions.

We first describe the coaxial collision problem and show that the equations of motion reduce to a planar Hamiltonian system of ordinary differential equations. We discuss the qualitative structure of the phase plane of this system and study the various bifurcations which occur. We give a complete bifurcation diagram and thus classify the behavior of the system in each region of the parameter space. We interpret these results in terms of the original physical system and show the possible types of collisions which occur. We discuss the implications for the overall effects of the collisions, noting the parameter regions where the finite size of the dipole can be neglected and the collisions can be viewed as classical particle collisions.

4.2 Coaxial Dipole System

In this section we apply the point vortex model of Chapter 2 to the case of two coaxial modons. We replace each modon with a pair of point vortices. The physical picture is illustrated in Figure 4.2. We refer to each vortex pair as a dipole. So we will really be looking at the interaction of two coaxial dipoles, each made up of two point vortices of equal and opposite strength. It is important that the dipoles have finite size since we are interested in the motion of the individual vortices during the collisions. We will refer to the strength of the dipoles in what follows, but by this we just mean the absolute value of the intrinsic circulation κ of each of the point vortices making up the dipoles. We give the complete equations from Section 2.2 for the motion of each point vortex and show that these equations reduce to a planar Hamiltonian system after a series of transformations.

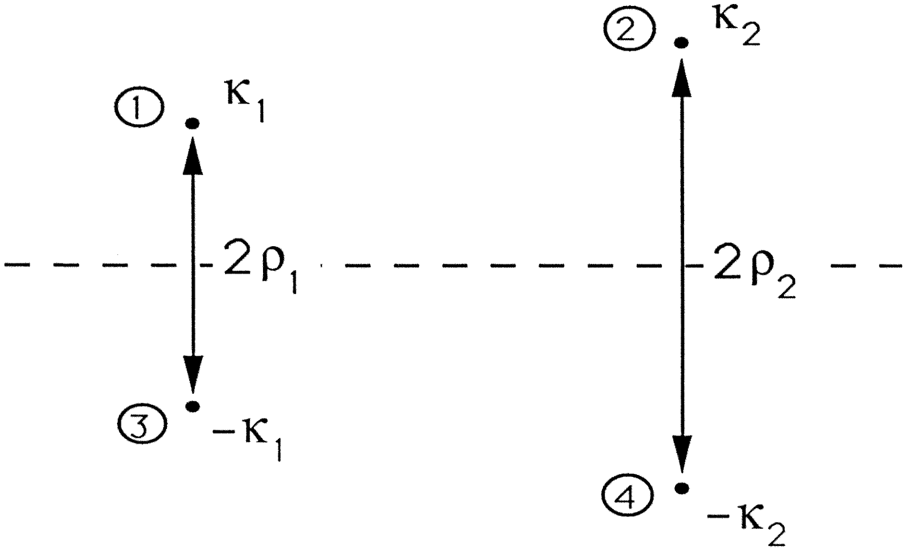

Figure 4.2 Geometry for the coaxial dipole system.

The dipoles have strengths κ_1^0 and κ_2^0 and the half-distances between vortices in each pair are ρ_1 and ρ_2 initially. The potential vorticity of each vortex is a useful quantity since it is constant. Using the initial values of κ and y in Figure 4.2, we have $q_1 = \kappa_1^0 + \beta\rho_1$ and $q_2 = \kappa_2^0 + \beta\rho_2$. The distances ρ_1 and ρ_2 must be positive. Due to the symmetry present in the problem we can always choose κ_1^0 to be positive while κ_2^0 can take on either sign. The dipoles are vertical initially and their centers lie on a common horizontal axis, chosen to be the x-axis here. We call such dipoles coaxial and note that the equations from the point vortex model imply that they will remain coaxial for all time. So the position of the lower vortex in each dipole is just the reflection across the x-axis of the position of the upper vortex. Hence we need only determine the motion of the upper two vortices, *i.e.* vortices 1 and 2 in Figure 4.2. The equations of motion for these vortices using the equations in (2.6) from Section 2.3 are

$$\begin{aligned}
\dot{x}_1 &= \frac{\gamma^2}{2\pi}\Big(2\kappa_1 y_1\zeta_{31} - \kappa_2(y_1 - y_2)\zeta_{21} + \kappa_2(y_1 + y_2)\zeta_{32}\Big) \\
\dot{x}_2 &= \frac{\gamma^2}{2\pi}\Big(2\kappa_2 y_2\zeta_{42} + \kappa_1(y_1 - y_2)\zeta_{21} + \kappa_1(y_1 + y_2)\zeta_{32}\Big) \\
\dot{y}_1 &= \frac{\gamma^2}{2\pi}\kappa_2(x_1 - x_2)(\zeta_{21} - \zeta_{32}) \\
\dot{y}_2 &= \frac{-\gamma^2}{2\pi}\kappa_1(x_1 - x_2)(\zeta_{21} - \zeta_{32})
\end{aligned} \tag{4.1}$$

where $\zeta_{ni} = K_1(\gamma r_{ni})/\gamma r_{ni}$ and $r_{ni} = |\mathrm{x}_n - \mathrm{x}_i|$. In what follows we will use the relation $\kappa_i = q_i - \beta y_i$, where q_i is constant, so that we can work with κ_i instead of y_i.

To determine the qualitative nature of the motion of the upper two vortices we do not need to know the complete motion of both vortices, we just need to know the motion of one of the vortices relative to the other. So we should expect that the qualitative nature of the motion will be described by two equations. We make several observations below which allow us to reduce the system of four equations in (4.1) to a planar system plus two equations which decouple from this system and can be solved trivially.

We first observe, using (2.5) and the expressions for $\dot{y}_1$ and $\dot{y}_2$ in (4.1), that we have $\kappa_1\dot{\kappa}_1 + \kappa_2\dot{\kappa}_2 = -\beta(\kappa_1\dot{y}_1 + \kappa_2\dot{y}_2) = 0$, so $\kappa_1^2 + \kappa_2^2$ is conserved. We can use this conserved quantity to reduce the equations for y_1 and y_2 to a single non-trivial equation. We use κ_1 and κ_2 and make the following transformation to the polar variables χ and θ :

$$\kappa_1 = \frac{\beta}{\gamma}\chi\cos\theta$$

$$\kappa_2 = \frac{\beta}{\gamma}\chi\sin\theta$$

Then $\chi = \gamma\sqrt{\kappa_1^2 + \kappa_2^2}/\beta$ is conserved, with the positive square root understood. So only the equation for θ will be non-trivial. Secondly, we note that x_1 and x_2 appear only in the form $x_1 - x_2$. So, we can further reduce the system by introducing scaled sum and difference variables $\bar{x}$ and ξ similar to those in Chapter 2:

$$\bar{x} = \gamma(x_1 + x_2)$$

$$\xi = \gamma(x_1 - x_2)$$

The equation for $\bar{x}$ will then decouple from the rest of the system because none of the equations depend on $\bar{x}$. For convenience we define the parameters $\delta_1 = \gamma q_1/\beta$ and $\delta_2 = \gamma q_2/\beta$. Finally, rescaling the time $\tau = (\gamma\beta/2\pi)t$ and the strengths $\tilde{\kappa}_i = \gamma\kappa_i/\beta$, the system (4.1) becomes

$$\frac{d\xi}{d\tau} = 2\tilde{\kappa}_1\tilde{y}_1\zeta_{31} - 2\tilde{\kappa}_2\tilde{y}_2\zeta_{42} - (\tilde{\kappa}_1 + \tilde{\kappa}_2)(\tilde{y}_1 - \tilde{y}_2)\zeta_{21} - (\tilde{\kappa}_1 - \tilde{\kappa}_2)(\tilde{y}_1 + \tilde{y}_2)\zeta_{32}$$

$$\frac{d\theta}{d\tau} = (\zeta_{21} - \zeta_{32})\xi \tag{4.2}$$

$$\frac{d\bar{x}}{d\tau} = 2\tilde{\kappa}_1\tilde{y}_1\zeta_{31} + 2\tilde{\kappa}_2\tilde{y}_2\zeta_{42} + (\tilde{\kappa}_1 - \tilde{\kappa}_2)(\tilde{y}_1 - \tilde{y}_2)\zeta_{21} + (\tilde{\kappa}_1 + \tilde{\kappa}_2)(\tilde{y}_1 + \tilde{y}_2)\zeta_{32}$$

$$\frac{d\chi}{d\tau} = 0$$

where

$$\tilde{\kappa}_1 = \chi\cos\theta$$

$$\tilde{\kappa}_2 = \chi\sin\theta$$

$$\tilde{y}_1 = \delta_1 - \tilde{\kappa}_1 = \delta_1 - \chi\cos\theta \tag{4.3}$$

$$\tilde{y}_2 = \delta_2 - \tilde{\kappa}_2 = \delta_2 - \chi\sin\theta$$

and $\zeta_{ni} = K_1(\tilde{r}_{ni})/\tilde{r}_{ni}$ with $\tilde{r}_{31} = 2\tilde{y}_1$, $\tilde{r}_{42} = 2\tilde{y}_2$, $\tilde{r}_{21}^2 = \xi^2 + (\tilde{y}_1 - \tilde{y}_2)^2$, $\tilde{r}_{32}^2 = \xi^2 + (\tilde{y}_1 + \tilde{y}_2)^2$.

Since χ is constant in time it can be viewed as a parameter in the remaining equations. The variable $\bar{x}$ can be obtained from ξ and θ by quadrature. So the system reduces to the planar system

$$\frac{d\xi}{d\tau} = f(\xi, \theta, \delta_1, \delta_2, \chi) = \frac{\partial H}{\partial \theta} \tag{4.4a}$$

$$\frac{d\theta}{d\tau} = g(\xi, \theta, \delta_1, \delta_2, \chi) = -\frac{\partial H}{\partial \xi} \tag{4.4b}$$

dependent upon the three parameters δ_1, δ_2, and χ. The system has a Hamiltonian H given by

$$H = K_0\big(\sqrt{\xi^2 + (\tilde{y}_1 - \tilde{y}_2)^2}\big) - K_0\big(\sqrt{\xi^2 + (\tilde{y}_1 + \tilde{y}_2)^2}\big) + F(\theta) \tag{4.5}$$

where

$$F(\theta) = \int_{\theta_0}^{\theta} (\tilde{\kappa}_1 K_1(2\tilde{y}_1) - \tilde{\kappa}_2 K_1(2\tilde{y}_2))d\theta'$$

The function K_0 is a modified Bessel function of the second kind. The functions f and g are just those in (4.2) and $\tilde{\kappa}_i$ and $\tilde{y}_i$ are replaced by their expressions in terms of θ and the parameters according to (4.3). Thus both functions f and g are 2π-periodic in θ.

The composite parameters of (4.4) can be related to the original physical parameters. The parameter χ is a measure of the combined strength of the two dipoles. The parameters δ_1 and δ_2 are sums of the strength and size of the individual dipoles. For weak dipoles, these are a good measure of the size of each dipole, while for strong dipoles they are a better measure of the strength of each. The ranges of the parameters are restricted by the assumption that some of the original parameters are positive. Note the δ_1 must be positive since ρ_1 and κ_1^0 were assumed to be positive while δ_2 can have either sign. Also, we can write $\chi^2 = (\delta_1 - \gamma\rho_1)^2 + (\delta_2 - \gamma\rho_2)^2$ using initial values and the definition of δ_1 and δ_2. Since ρ_2 is positive, we must have $\chi > -\delta_2$ if $\delta_2 < 0$. So χ must satisfy $\chi > \max(0, -\delta_2)$.

The qualitative features of the coaxial dipole system may be inferred directly from a knowledge of the behavior of (4.4) in the ξ-θ plane as a function of the parameters δ_1, δ_2, and χ. We proceed by studying the nature of the phase space in the ξ-θ plane and several types of singularities which can occur. We then study the various bifurcations that can occur in parameter space. By determining exactly where all the bifurcations occur we can divide the parameter space into different sections. Each section then corresponds to a different qualitative state of the ξ-θ

system. In this way we can catalogue the various states of the system in the different regions of parameter space.

4.3 Structure of the Phase Plane

In this subsection we discuss the general structure of phase plane diagrams for the system (4.4) and some limitations on the ranges of validity of (4.4) in the ξ-θ plane. The system is 2π-periodic in θ, so any horizontal strip of height 2π in the ξ-θ plane will suffice to study the system in general. The remainder of the ξ-θ phase plane then consists of copies of this strip. Since the structure of the phase plane changes as parameters change, we will find it convenient to choose an appropriate 2π-strip for each choice of parameters. This is just so that the edges of the strip do not cut through identifiable structures in the phase plane.

The physical constraints that $y_1 > 0$ and $y_2 > 0$ can restrict the values of θ within each strip which are physically valid. So, for some values of the parameters we will see that the appropriate 2π-strip in the ξ-θ plane will be sliced horizontally into smaller strips, corresponding to regions of physically valid or invalid θ. These gaps in allowable θ are simply artifacts of the transformations we have used and do not indicate any unphysical behavior. We know from (4.3) that $\tilde{y}_1 = \gamma y_1 = \delta_1 - \chi \cos\theta$ and $\tilde{y}_2 = \gamma y_2 = \delta_2 - \chi \sin\theta$. Hence any physically valid θ must satisfy

$$\cos\theta < \frac{\delta_1}{\chi} \qquad \text{and} \qquad \sin\theta < \frac{\delta_2}{\chi}$$

Since $\delta_1 > 0$ and $\delta_2 > -\chi$ there will always be some region of valid θ around

$\theta = -\pi/2$. If $\delta_1 > \chi$ and $\delta_2 > \chi$ then all values of θ are valid. In the case that $\chi < \sqrt{\delta_1^2 + \delta_2^2}$, $\chi > \delta_1$, $\chi > \delta_2$, and $\delta_2 > 0$ there are two disjoint horizontal strips of valid θ contained within the appropriate 2π-strip. In the remainder of the parameter space there is a single strip of valid θ within the 2π-strip.

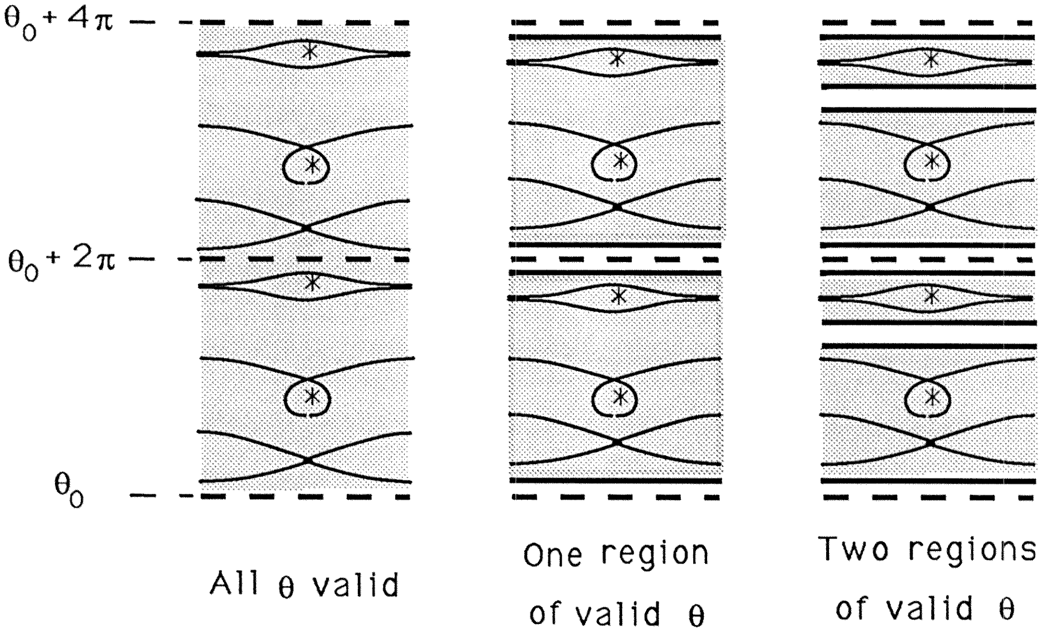

Figure 4.3 Three different types of phase planes possible. The shaded areas are the allowable regions of the ξ-θ plane.

The three cases are illustrated in Figure 4.3 with example phase portraits. Singular horizontal walls form the boundaries of the valid ranges of θ in the latter two cases. All the possible states of the ξ-θ system will have phase portraits with domains similar to one of the three shown in Figure 4.3. The flow between the walls may be different, however. The walls correspond physically to one of the dipoles having zero size and shooting off horizontally with infinite speed. Some of the bifurcations in the system consist of structures such as fixed points or separatrices appearing or disappearing through these singular walls.

In addition to these wall singularities, point singularities corresponding physically to the upper two point vortices having the same position can occur. This happens when $\xi = 0$ and $y_1 = y_2$. So θ must satisfy $\delta_1 - \chi \cos\theta = \delta_2 - \chi \sin\theta$ or

$$\cos(\theta + \frac{\pi}{4}) = \frac{\delta_1 - \delta_2}{\sqrt{2}\chi} \equiv \nu \tag{4.6}$$

For $|\nu| < 1$ there are two values of θ in each 2π-strip corresponding to point singularities at $\xi = 0$. For $|\nu| > 1$ there are no point singularities. So two point singularities merge and disappear as $|\nu|$ increases through 1.

4.4 Analysis of Bifurcations

In this section we study the various bifurcations which occur in the system (4.4) as parameters are changed. One class of bifurcations are those involving wall or point singularities. These can be studied analytically. A second class are those involving just fixed points. We will see that the only such bifurcation in (4.4) is the saddle-node bifurcation of two fixed points. We find the curves in parameter space on which this bifurcation occurs numerically using the bifurcation software package AUTO (Doedel and Kernevez [1986]). The last class of bifurcations involve separatrices, not just fixed points or singularities. These are known loosely as homoclinic bifurcations and can be found numerically with the AUTO software by making use of the Hamiltonian for the system.

The bifurcations only involving wall singularities can be determined from the discussion in Section 4.3. Since walls form the boundaries of regions of valid θ in the ξ-θ phase plane, two walls must merge when the number of valid regions of θ changes. Thus two walls merge when $\chi = \sqrt{\delta_1^2 + \delta_2^2}$ and $\delta_2 > 0$, since the number of valid regions of θ changes there. For the same reason, two walls must merge when $\chi = \delta_1$ with $\delta_2 > 0$ and when $\chi = \delta_2$ with $\delta_2 > 0$.

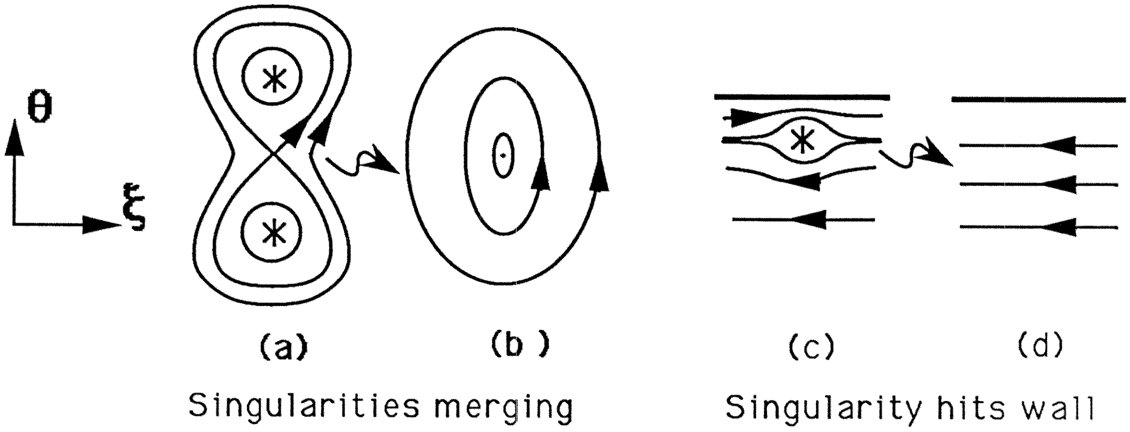

Figure 4.4 Bifurcations involving singularities.

The surface in parameter space corresponding to the merging of two point singularities in the phase space can be found using (4.6). Since the merging takes place when $|\nu| = 1$ and since χ must be positive, this surface is given by

$$\chi = \chi_m(\delta_1, \delta_2) = \frac{|\delta_1 - \delta_2|}{\sqrt{2}}. \tag{4.7}$$

A point singularity can pass through a wall singularity as a parameter changes. This occurs when $\xi = 0$ and $y_1 = y_2 = 0$. So $\delta_1 = \chi \cos\theta$ and $\delta_2 = \chi \sin\theta$. Hence a necessary condition for a point singularity to pass through a wall singularity in phase space is that the parameters lie on the surface defined by

$$\chi = \chi_w(\delta_1, \delta_2) = \sqrt{\delta_1^2 + \delta_2^2}. \tag{4.8}$$

Typical phase space portraits of these two bifurcation are shown in Figure 4.4.

The merging of two point singularities, which occurs from frame (a) to frame (b) in Figure 4.4, appears very similar to a pitchfork bifurcation. The merging centers in this case are point singularities, not fixed points, and we have used a '*' to represent each. The disappearance of a point singularity through a singular wall is shown in frames (c) and (d). Note that the point singularity in frame (c) is enclosed by an eye-like structure. This structure disappears through the wall along with the point singularity.

A fixed point can also pass through a wall singularity as a parameter changes. The details of the analysis for this bifurcation are straightforward and tedious, so we present only the results. With the assumption that δ_1 is positive, this bifurcation occurs only when $\delta_2 = 0$ with singular walls at $\theta = 0$ and $\theta = \pi$ corresponding to $y_2 = 0$. For $\chi < \delta_1$, we define the positive constant $\zeta_0 = 2\chi(2K_1(\delta_1 - \chi) - K_1(2(\delta_1 - \chi)))$. For $0 < \zeta_0 < 1$, a center appears through the wall at $\theta = 0$ and a saddle appears through the wall at $\theta = -\pi$ as δ_2 increases through 0. For $\zeta_0 > 1$, a saddle disappears through the wall at $\theta = 0$ and a saddle appears through the wall at $\theta = -\pi$ as δ_2 increases through 0. For $\chi > \delta_1$ there is no fixed point near $\theta = 0$, but the saddle still appears through $\theta = -\pi$ as δ_2 increases through 0.

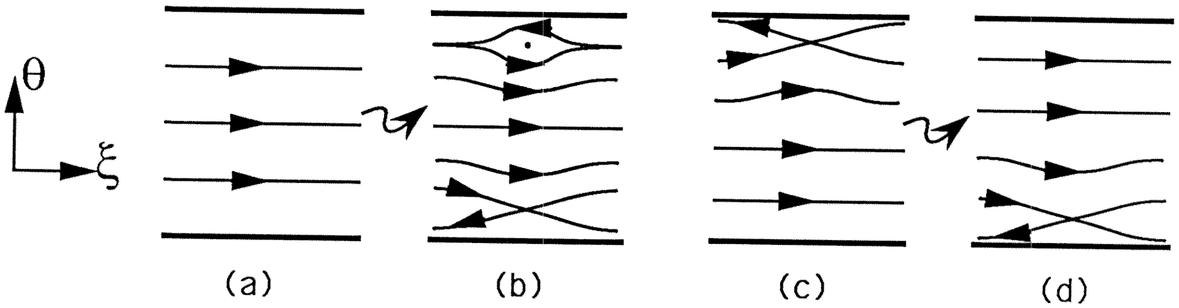

Figure 4.5 Bifurcations in which fixed points pass through singular walls.

Figure 4.5 shows pictures of the phase plane before and after fixed points pass through walls. Frames (a) and (b) show the center at $\theta = 0$ and the saddle at $\theta = -\pi$ appearing as δ_2 increases through 0. We note that the center which appears in frame (b) is the heart of an infinitely long eye-like structure, mentioned earlier. The outer edges of this eye are the limits of periodic orbits inside the eye and separate the bounded inner flow from the unbounded outer flow. These separatrices approach one another as $\xi \to \pm\infty$. This structure seems to be the only possible one which is consistent with the appearance of a center through a singular wall. It resembles a localized vortical disturbance on the stagnation line of a horizontal shear flow. Frames (c) and (d) show the saddle at $\theta = 0$ disappearing and the saddle at $\theta = -\pi$ appearing as δ_2 increases through 0.

A second type of bifurcation that can occur only involves fixed points. The only such bifurcation that we have found in (4.4) is the saddle-node bifurcation between two fixed points. For conservative systems such as (4.4), a saddle-node bifurcation occurs when two fixed points, one of saddle type and the other of center type, merge and disappear as a parameter passes through a critical value. At the critical value of the parameter, there is a single degenerate fixed point. In terms of the functions f and g in (4.4), we must have $f = g = 0$ and $f_\xi g_\theta - g_\xi f_\theta = 0$ at such a point. This only occurs when $\xi = 0$ and θ is such that $f(0, \theta, \delta_1, \delta_2, \chi) = 0$ and $f_\theta(0, \theta, \delta_1, \delta_2, \chi) = 0$. Of course this will only be possible in general if the parameters lie on a particular two-dimensional surface in the three-dimensional parameter space. We have found particular values $\theta^c, \delta_1^c, \delta_2^c, \chi^c$ at which a saddle-node bifurcation occurs by looking at the fixed points of (4.4) as functions of the parameters. We fixed δ_1 and followed a curve $\theta^c(\delta_2), \chi^c(\delta_2)$ on which $f = f_\theta = 0$ using the arclength continuation software package AUTO. This allowed us to trace out curves in parameter space on the saddle-node bifurcation surface. So we can picture this surface by drawing various slices of it. We show one such slice in the next section.

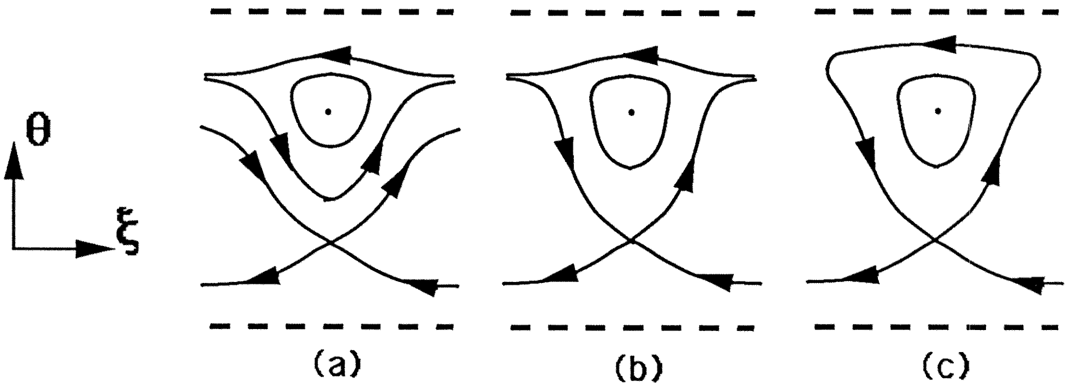

Figure 4.6 An example of a homoclinic bifurcation.

A final class of bifurcations is that of the homoclinic bifurcations. These are bifurcations involving the coalescence of separatrices. One example is shown in Figure 4.6. As a parameter is varied, the saddle separatrix moves upward to join with the eye separatrix. The separatrices partially annihilate one another leaving only a saddle-node loop separatrix. We can follow these bifurcations numerically in much the same way as we followed the saddle-node bifurcation by making use of the Hamiltonian H, given in (4.5). We know that H is constant along orbits, so we can find the value of H on a separatrix by finding the value at a specific point on the separatrix. In the case shown in Figure 4.6, the value of the Hamiltonian on the separatrix emanating from the saddle is just its value at the saddle. This value is $H(0, \theta_1, \delta_1, \delta_2, \chi)$ where θ_1 is the value of θ at the saddle. Similarly, the value of the Hamiltonian on the eye separatrix is just its value at the extreme right or left edges of the eye. This value is $H(\pm\infty, \theta_2, \delta_1, \delta_2, \chi)$ where θ_2 is the value of θ on the eye at $\xi = \pm\infty$. When the two separatrices coalesce, the Hamiltonian must have the same value on both. Thus the equations specifying this bifurcation are

$$f(0, \theta_1, \delta_1, \delta_2, \chi) = 0$$

$$f(\pm\infty, \theta_2, \delta_1, \delta_2, \chi) = 0$$

$$H(0, \theta_1, \delta_1, \delta_2, \chi) = H(\pm\infty, \theta_2, \delta_1, \delta_2, \chi)$$

Again we found one such set of values $\theta_1^c, \theta_2^c, \delta_1^c, \delta_2^c, \chi^c$ and then followed a curve of such points as a function of δ_2 for a fixed value of δ_1 using AUTO. This curve will be shown in the next section. Similar curves corresponding to other homoclinic bifurcations which occur are also presented there.

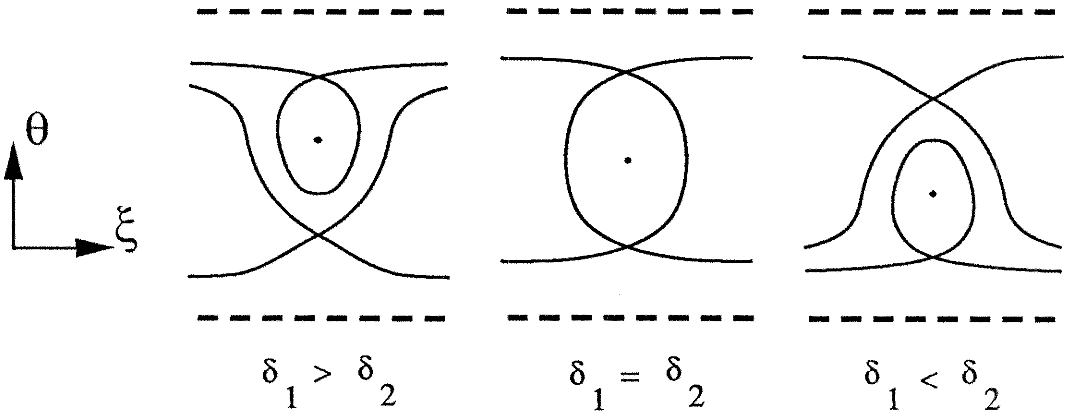

Figure 4.7 Homoclinic bifurcation forced by vertical symmetry.

One curve in parameter space along which homoclinic bifurcations can take place can be found very simply by noting a symmetry of the system. We note that when $\delta_1 = \delta_2$, the system (4.4) is symmetric with respect to θ about $\theta = -\pi/4$. This symmetry forces otherwise nonsymmetric configurations in the phase plane to merge in order to form symmetric configurations. An example is shown in Figure 4.7. The configurations of separatrices for $\delta_2 < \delta_1$ and $\delta_2 > \delta_1$ cannot be deformed in any way to form a vertically symmetric configuration except through the coalescence of two of the separatrices at $\delta_2 = \delta_1$. Thus the surface $\delta_1 = \delta_2$ will correspond to homoclinic bifurcations whenever the symmetry requirements cannot be met otherwise.

4.5 Bifurcation Diagram for the Planar System

In this section we present the results of a complete study of the bifurcations that occur in (4.4) for various values of the parameters δ_1, δ_2, and χ. We have chosen to present a single slice of the parameter space with δ_1 fixed. This yields a planar bifurcation diagram in the parameters δ_2 and χ. The curves on which bifurcations occur break this diagram into distinct regions corresponding to different qualitative behaviors in the phase plane. Along with this bifurcation diagram we give phase portraits corresponding to each of the regions in the diagram. Thus we classify the qualitative behavior of (4.4) in each region of the δ_2-χ plane for a fixed value of δ_1. We then note that this slice is representative of the entire parameter space, differing from other such slices in a very minor way.

The complete bifurcation diagram is given in Figure 4.8. We have chosen the slice with $\delta_1 = 10$. The curves on which bifurcations of (4.4) take place are plotted in the δ_2-χ plane. As noted in Section 4.2, the parameter δ_2 is unrestricted while χ must satisfy $\chi > \max(0, -\delta_2)$. So the shaded region in the lower left corner of Figure 4.8 with $\chi < -\delta_2$ is not physically valid. Superimposed on the shaded region is a magnification of the dense region around $\delta_2 = 0$ outlined by the dotted line. Each curve in Figure 4.8 is labeled according to the type of bifurcation which occurs on it. Two of the lines, $\chi = \delta_1$ and $\chi = \delta_2$, are each broken into a solid and a dashed segment. These segments correspond to different bifurcations so we changed the line type for clarity.

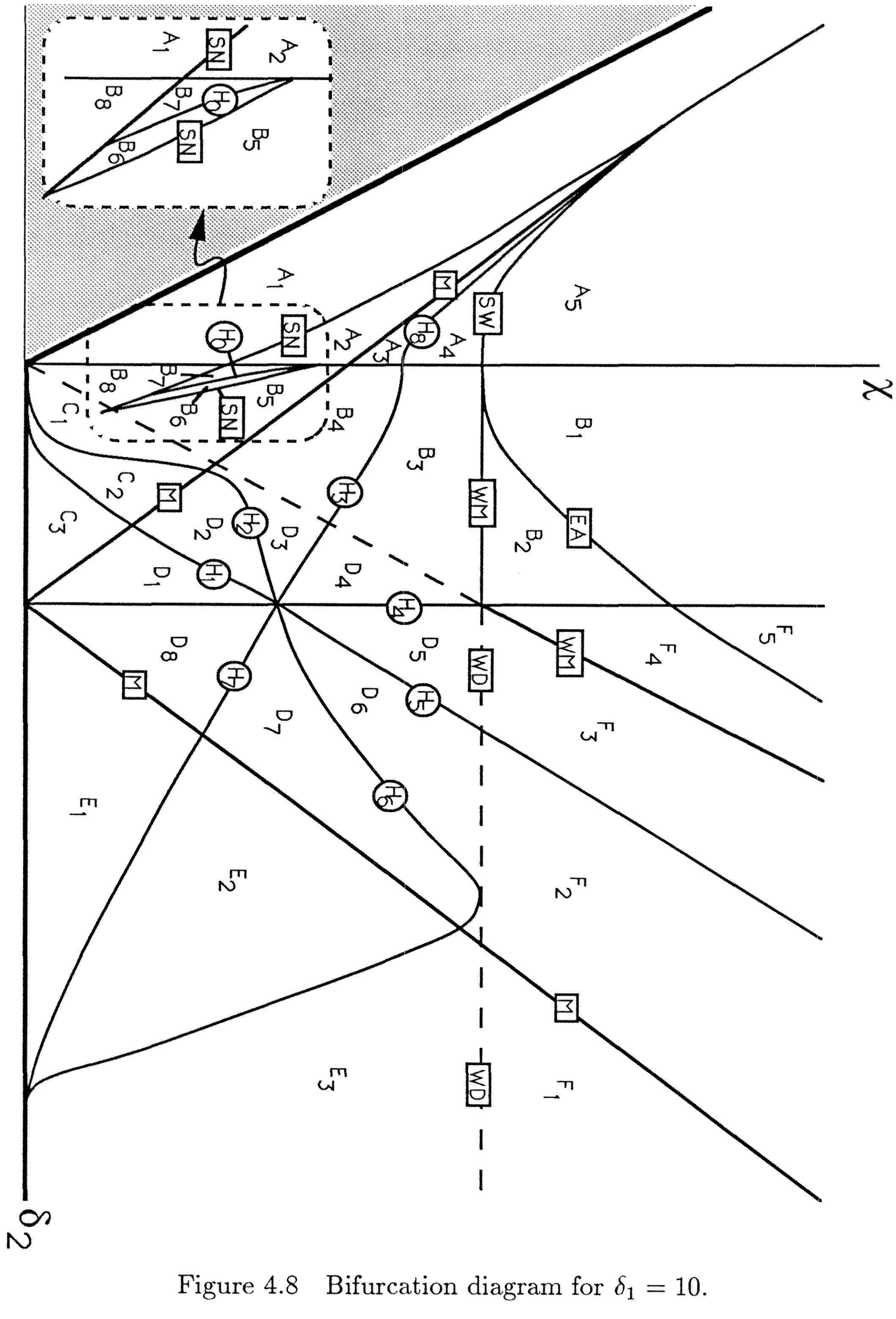

Figure 4.8 Bifurcation diagram for $\delta_1 = 10$.

The curves involving point singularities and fixed points are labeled simply. The curve on which a saddle-node bifurcation occurs is labeled SN. The curve on which two point singularities merge is labeled M. This curve is just a plot of $\chi = \chi_m$ in (4.7) for $\delta_1 = 10$. The curve SW is where a point singularity hits a wall singularity. This curve is given by $\chi = \chi_w$ in (4.8).

The curves where wall singularities merge are labeled to reveal more information about what happens on each segment. The curve labeled EA corresponds to the appearance of two walls in the middle of a valid region of θ in the ξ-θ phase plane as χ is decreased. The eye structure around a point singularity lies between these two walls. Thus at this point an eye structure appears. The two segments labeled WM correspond to two walls merging and disappearing as χ is decreased. Here the two separate regions of valid θ join to form one region of valid θ. The two segments labeled WD correspond to the two walls disappearing altogether. Actually, the two walls here merge with their counterparts in the 2π-slices above and below them in the ξ-θ plane. This leaves all values of θ valid after χ decreases through either of these segments.

The curves along which homoclinic bifurcations occur are all labeled H_i, each one being distinguished by its index i. Although some of the curves appear to be continuous and smooth when they cross other lines, some of the segments may be labeled differently because they actually correspond to different homoclinic bifurcations. On H_0, H_2, H_3, and H_5 a saddle loop separatrix coalesces with an eye separatrix. On H_1 and H_7 a saddle loop separatrix makes a transition from being bounded in θ to being unbounded in θ. On H_4 a saddle loop separatrix coalesces with a saddle separatrix. On H_6 and H_8 a saddle separatrix coalesces with an eye separatrix.

The bifurcation diagram in Figure 4.8 is representative of the entire parameter space. That diagram is plotted for $\delta_1 = 10$, but the same diagram plotted for other values of δ_1 which are positive would appear almost identical in structure. All the curves shown in Figure 4.8 exist for all $\delta_1 > 0$. They cross each other in exactly the same way topologically for all δ_1 except for the saddle-node bifurcation curve SN. This curve crosses the χ-axis in two places in Figure 4.8. The higher of these two crossings occurs below the curve labeled M when $\delta_1 < 10.78$ and above that curve when $\delta_1 > 10.78$. So, for $\delta_1 < 10.78$ the curves SN and M in Figure 4.8 do not cross. For $\delta_1 > 10.78$ these two curves do cross. Thus all slices of the parameter space with fixed δ_1 will be very similar to the slice shown in Figure 4.8. A few other regions will be introduced when the curves SN and M cross, but no new qualitative behaviors will be added.

We now discuss what happens in the ξ-θ phase plane corresponding to each region of parameter space. Each region which lies between bifurcation curves corresponds to a particular qualitative behavior of the system (4.4). The various regions have been labeled A_1, A_2, A_3, ..., F_3, F_4, F_5 for reference. Figure 4.9 shows the phase portraits corresponding to the various regions. Each bifurcation which occurs

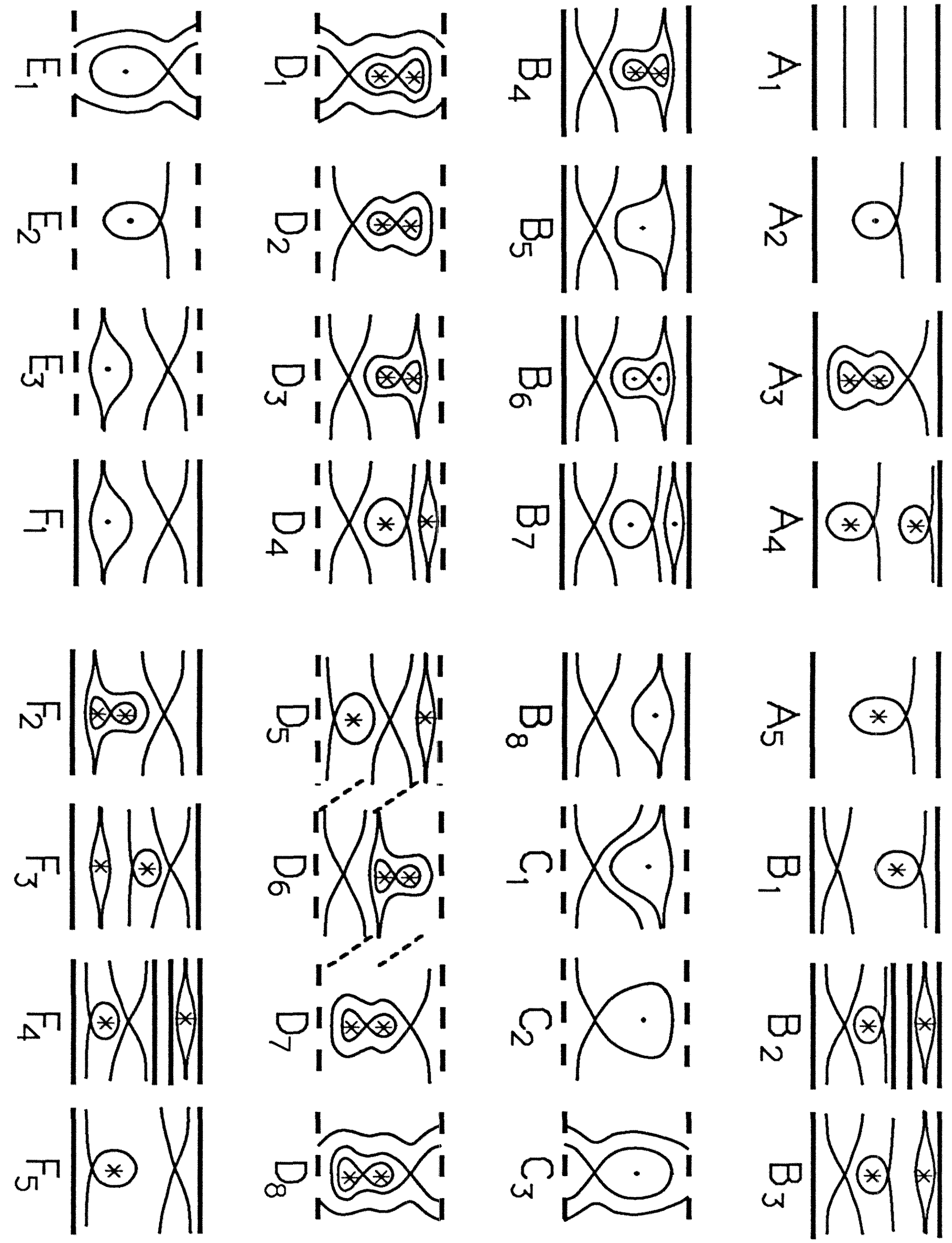

Figure 4.9 Phase portraits for each parameter region in Figure 4.8.

can be seen by comparing the appropriate phase portraits in Figure 4.9 for the regions on either side of the curve for that bifurcation. Neighboring phase portraits are drawn on comparable horizontal strips in the ξ-θ plane in general. The plots in D_5, D_6, and D_7 are in different strips so that the structures shown are not cut by the boundary lines of the 2π-strips. We have indicated these shifts with slanted dashed lines in Figure 4.9.

We have chosen to show only fixed points, singularities, and separatrices in the phase portraits. The qualitative nature of all the other orbits follows from a knowledge of these special orbits. The arrows indicate the direction of flow. The dots in Figure 4.9 correspond to fixed points of center type. Saddle fixed points are not highlighted except that they exist wherever orbits intersect. Each point singularity is represented by a '$*$' while each wall singularity is represented by a dark horizontal line. The normal solid lines in Figure 4.9 are separatrices. The horizontal dashed lines at the top and bottom of some portraits are the imaginary boundaries of the 2π-strip chosen for those portraits.

4.6 Physical Interpretation of Results

In this section we interpret the results of the previous section on the planar system in terms of the original coaxial dipole system. We discuss the different types of interactions that occur. We also discuss the implications for the coaxial modon system and the general problem of collisions between modons.

Each phase portrait in Figure 4.9 contains a variety of orbits. Each of these orbits of the planar system (4.4) corresponds to a particular type of behavior in the original physical system (4.1). The correspondences are rather straightforward except for determining the behavior of the quantity $\bar{x}$ in (4.2). Recall that $\bar{x} = \gamma(x_1 + x_2)$ is just γ times twice the horizontal centroid of the coaxial dipole system. So we can determine the relative motion of the dipoles without a knowledge of $\bar{x}$. Thus the qualitative behavior of the system (4.1) will be the relevant qualitative behavior corresponding to that found in (4.4) plus an overall translation of the whole system horizontally. Although the rate of this overall translation may vary in time, it is not important in understanding the qualitative behavior of the coaxial dipole system.

The simplest motion may be seen in the portrait for region A_1 in Figure 4.9. All orbits there pass from left to right without significant deflection vertically. Thus the angle θ is roughly constant along such orbits. The variable ξ, which is the signed horizontal distance between the dipoles, increases monotonically from $-\infty$ to $+\infty$. Such an interaction is a clean collision between the dipoles in which one dipole simply passes between the two vortices in the other dipole. Figure 4.10 shows a schematic of this motion in frame (a). This figure shows only the motion of the two upper vortices in each pair. The lower vortices are just the mirror reflections of these upper vortices through the horizontal axis shown in each frame of Figure 4.10. Note that the symmetry of (4.4) with respect to ξ guarantees that the dipoles will return to exactly the same size and strength after the collision as before the collision. All coaxial collisions in which the dipoles pass by one another so that ξ goes from $+\infty$ to $-\infty$ are conservative.

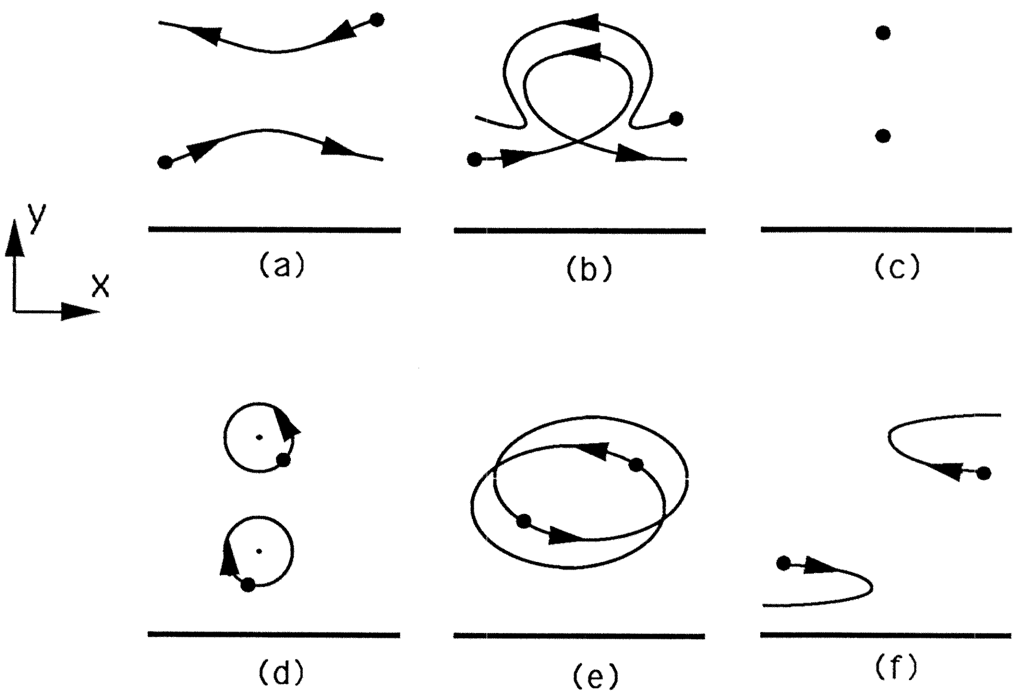

Figure 4.10 Physical motions exhibited by upper two vortices in the coaxial dipole system.

A slight variation of this type of behavior can be seen in region A_2. The orbits which pass just below the saddle loop will travel horizontally to the right until they approach the bounded portion of the loop. They will then dip down around the loop and eventually appear on the right side outside the loop traveling to the right again. Thus the upper point vortices approach one another at first and then change their heights quite a bit during the close interaction. They finally emerge traveling away from one another with their sizes and strength conserved. This motion is diagrammed in frame (b) of Figure 4.10. This corresponds to the type of modon collision show in Figure 4.1.

The portrait in region A_2 also contains two fixed points. These correspond to equilibrium configurations of the system (4.4). In terms of the original coaxial two dipole system (4.1), this corresponds to the two dipoles having constant size and strength and being lined up vertically on the y-axis. This is shown in frame (c) of Figure 4.10. This entire configuration may move horizontally with constant speed, but it is at rest in the appropriate frame of reference. The question naturally arises as to the stability of the equilibria. One of the fixed points is a saddle, and is thus unstable, *i.e.*, any perturbation of the point vortices away from their equilibrium position will grow exponentially in time. The other fixed point is a center, corresponding to a stable equilibrium configuration of the point vortices.

The periodic motions around the center fixed point lie inside the saddle loop in the portrait for region A_2. The orbits inside the loop are periodic and symmetric about $\xi = 0$. This corresponds to the two upper point vortices oscillating periodically about their equilibrium position corresponding to the center fixed point. This motion is shown in frame (d) of Figure 4.10. The two lower point vortices, which are the reflections of the upper vortices across the x-axis in Figure 4.2, also oscillate periodically. While the individual vortices oscillate, the center of the system translates horizontally.

The phase portrait in region A_3 introduces another type of behavior. The portrait in A_3 is the same as that of A_2 except that the center fixed point has undergone the pitchfork-like bifurcation discussed in Section 4.4. The center has split into a saddle sandwiched between two singular centers. The singular centers, each denoted by a '$*$' in the phase portraits, are the point singularities discussed in Sections 4.3 and 4.4. The orbits around the point singularities are qualitatively similar to those around a normal center. The speed at which these orbits are traced out approaches infinity close to the singular center, however. Physically, this corresponds to the two upper point vortices starting very close to one another and orbiting each other very quickly. The periodic orbits around these point singularities correspond to the upper two vortices orbiting one another in a 'leap frog' fashion as the center of the dipole system translates horizontally. This motion is shown in frame (e) of Figure 4.10 and was observed by Love [1894] in his study of interactions between coaxial pairs of point vortices for the Euler equations.

A consideration of the phase portrait for region C_1 uncovers two more types of behaviors. The eye at the top of C_1 encloses a band of periodic orbits. These orbits become stretched horizontally and pinched at the left and right edges as they approach the eye separatrix. These correspond to highly noncircular oscillations of the point vortices about their equilibrium positions, which correspond to the center fixed point in the middle of C_1. Another behavior is that of the semi-bounded orbits in the left or right regions defined by the saddle separatrices. These orbits start from $\xi = \pm\infty$ at a finite value of θ, approach the saddle and then turn around to return to $\xi = \pm\infty$ and a different value of θ. These correspond to the two dipoles approaching one another and then bouncing off and traveling away from one another. Their heights change appreciably during their close interaction causing their horizontal velocities to change sign. This is shown in frame (f) of Figure 4.10.

For the specific problem of dipoles initially far apart colliding, only the motions in which ξ is unbounded are of interest. The collisions shown in Figure 4.10 (a), (b), and (f) are the only such collisions. The collisions in (a) and (b) are conservative since ξ passes from $+\infty$ to $-\infty$ and the system (4.4) is symmetric with respect to ξ. The dipoles pass by one another and return to their original sizes, strengths, and speeds after such collisions. The collision in (f) is not conservative since ξ starts at $+\infty$ and eventually returns there after the collision. The dipoles bounce off one another in such a collision and the sizes and strengths are in general different from their original values afterward.

The conservative collisions correspond to orbits in the phase portraits in Figure 4.9 which pass from one side of a portrait to the opposite side. Such orbits occur for all initial conditions at the extreme left or right of each diagram which contains no solitary saddle separatrix. In the cases where a solitary saddle separatrix exists, the initial conditions contained inside either the right or left semi-infinite quadrants of the separatrix will result in the nonconservative rebounding collisions. The system

(4.4) exhibits a solitary saddle separatrix in many of the portraits in Figure 4.9. These separatrices occur in regions of parameter space corresponding to overtaking collisions of strong dipoles, in which the dipoles initially travel in the same direction. Head-on collisions, in which the dipoles travel in opposite directions initially, appear to be conservative for all initial conditions. Owing to the presence of the saddle separatrices, overtaking collisions are nonconservative for some initial conditions, but conservative for all others.

4.7 Conclusions

In this chapter we studied the problem of the coaxial collision of two modons using the point vortex model. We modeled the two modons by two pairs of point vortices and showed that the resulting equations were a planar Hamiltonian system which could be studied in detail. We found the various possible interactions between the two pairs of point vortices and interpreted them physically. We found several collision-type interactions as well as well as bound periodic motions. The implications for the classical particle collision problem of two particles initially very far apart were considered. We found that in general the collisions would appear to be clean in the sense that one dipole would pass through the other and the two dipoles would resume their original sizes, strengths, and speeds afterwards. In some cases, associated with overtaking collisions in which the dipoles travel in the same direction initially, the dipoles could bounce off one another and return in the direction from which they originated. In these cases, the collisions are nonconservative in the sense that the dipoles do not return to their original sizes or speeds.

References

Aref, H. and Pomphrey, N. (1982). Integrable and chaotic motions of four vortices. *Proceedings of the Royal Society of London, A*, **380**, 359–387.

Arnold, V. I. (1965). Conditions for nonlinear stability of the stationary plane curvilinear flows of an ideal fluid. *Dokl. Mat. Nauk SSSR*, **162**, 773–777.

Byrd, P. F. and Friedman, M. D. (1954). *Handbook of Elliptic Integrals for Engineers and Scientists*. Springer Verlag, Berlin.

Carnevale, G. F. *et al.* (1988a). Numerical experiments on modon stability to topographic perturbations. *Physics of Fluids*, **31**, 2562–2566.

Carnevale, G. F. *et al.* (1988b). The role of initial conditions in flow stability with an application to modons. *Physics of Fluids*, **31**, 2567–2572.

Charney, J. G. (1948). On the scale of atmospheric motions. *Geofysiske Publikasjoner*, **17**, 3–17.

Doedel, E. J. and Kernevez, J. D. (1985). Software for continuation and bifurcation problems. *Applied Math. Technical Report*, Caltech.

Flierl, G. R., Larichev, V. D., McWilliams, J. C., and Reznik, G. M. (1981). The dynamics of baroclinic and barotropic solitary eddies. *Dynamics of Atmospheres and Oceans*, **5**, 1–41.

Flierl, G. R., Stern, M. E., and Whitehead, J. A. (1983). The physical significance of modons: laboratory experiments and general integral constraints. *Dynamics of Atmospheres and Oceans*, **7**, 233–263.

Fischer, B. and Kramer, M. (1989). Experimental study of drift wave turbulence and anomalous transport. *Plasma Physics and Controlled Fusion*, **31**, 453–470.

Gourlay, A. R. and Morris, J. L. (1970). On the comparison of multistep formulations of the optimized Lax-Wendroff method for nonlinear hyperbolic systems in two space variables. *Journal of Computational Physics*, **5**, 229–243.

Guckenheimer, J. and Holmes, P. (1983). *Nonlinear Oscillations, Dynamical Systems, and Bifurcations of Vector Fields.* Springer Verlag, New York.

Hasegawa, A., Maclennan, C. G., and Kodama, Y. (1979). Nonlinear behavior and turbulence spectra of drift waves and Rossby waves. *Physics of Fluids*, **22**, 2122–2129.

Hasegawa, A. and Mima, K. (1977). Stationary spectrum of strong turbulence in magnetized uniform plasma. *Physical Review Letters*, **39**, 205–208.

Hasegawa, A. and Mima, K. (1978). Pseudo three-dimensional turbulence in a magnetized nonuniforn plasma. *Physics of Fluids*, **21**, 87–92.

Hazeltine, R. D. (1983). Reduced magnetohydrodynamics and the Hasegawa-Mima equation. *Physics of Fluids*, **26**, 3242–3245.

Hogg, N. G. and Stommel, H. M. (1985). The heton, an elementary interaction between discrete baroclinic geostrophic vortices, and its implications concerning eddy heat flow. *Proceedings of the Royal Society of London, A*, **397**, 1–20.

Horton, W., Liu, J., Meiss, J. D., and Sedlak, J. E. (1986). Solitary vortices in a rotating plasma. *Physics of Fluids*, **29**, 1004–1010.

Jovanovic, D., (1988). Short wavelength drift-Alfven vortices. *Physica Scripta*, **38**, 400–403.

Laedke, E. W. and Spatschek, K. H. (1985). Dynamical properties of drift vortices. *Physics of Fluids*, **28**, 1008–1010.

Larichev, V. D. and Reznik, G. M. (1976). Two-dimensional solitary Rossby waves. *Dokl. Akad. Nauk SSSR*, **231**, 12–13.

Larichev, V. D. and Reznik, G. M. (1983). On collisions between two-dimensional solitary Rossby waves. *Oceanology*, **23**, 545–552.

Liewer, P. C. (1985). Measurements of microturbulence in tokamaks and comparisons with theories of turbulence and anomalous transport. *Nuclear Fusion*, **25**, 543–621.

Love, A. E. H. (1894). On the motion of paired vortices with a common axis. *Proceedings of the London Mathematical Society*, **25**, 185.

Makino, M., Kamimura, T., and Sato, T. (1981). Two-dimensional behavior of solitons in a low-beta plasma with convective motion. *Journal of the Physical Society of Japan*, **50**, 954–961.

Makino, M., Kamimura, T., and Taniuti, T. (1981). Dynamics of two-dimensional solitary vortices in a low-beta plasma with convective motion. *Journal of the Physical Society of Japan*, **50**, 980–989.

McWilliams, J. C. (1983). Interactions of isolated vortices, II. Modons generated by monopole collisions. *Geophysical and Astrophysical Fluid Dynamics*, **24**, 1–22.

McWilliams, J. C. and Zabusky, N. J. (1982). Interactions of isolated vortices, I. Modons colliding with modons. *Geophysical and Astrophysical Fluid Dynamics*, **19**, 207–227.

McWilliams, J. C. *et al.* (1981). Numerical studies of barotropic modons. *Dynamics of Atmospheres and Oceans*, **5**, 219–238.

Mikhailovskii, A. B. *et al.* (1984). Ballooning vortex in a magnetized plasma. *Physics Letters A*, **100**, 503–506.

Mikhailovskii, A. B. *et al.* (1984). Alfven vortex solution in a homogeneous magnetized plasma. *Physics Letters A*, **101**, 263–265.

Mikhailovskii, A. B. *et al.* (1984). Short wavelength drift vortices. *Physics Letters A*, **104**, 94–86.

Mikhailovskii, A. B. *et al.* (1984). Electro drift solitons in an inhomogeneous magnetized plasma. *Physics Letters A*, **105**, 48–50.

Morikawa, G. K. and Swenson, E. V. (1971). Interacting motion of rectilinear geostrophic vortices. *Physics of Fluids*, **14**, 1058–1073.

Pecseli, H. L., Rasmussen, J. J., and Thomsen, K. (1984). Nonlinear interaction of convective cells in plasmas. *Physical Review Letters*, **52**, 2148–2151.

Pedlosky, J. (1979). *Geophysical Fluid Dynamics.* Springer-Verlag, New York, Berlin, Heidelberg, Tokyo.

Rom-Kedar, V., Leonard, A., and Wiggins, S. (1990). An analytical study of transport, mixing and chaos in an unsteady vortical flow. *Journal of Fluid Mechanics*, to appear.

Sakuma, H. and Ghil, M. (1990) Stability of stationary barotropic modons by Lyapunov's direct method. *Journal of Fluid Mechanics*, **211**, 393–416.

Shukla, P. K., Pecseli, H. L., and Rasmussem, J. J. (1986). Electromagnetic drift modes in an inhomogeneous electron gas. *Physical Review A*, **33**, 1398–1401.

Shukla, P. K., Spatschek, K. H., and Balescu, R. (1985). Nonlinear convective cell equations and dipole vortex solutions in homogeneous magnetoplasmas. *Physics Letters A*, **107**, 461–464.

Shukla, P. K. and Yu, M. Y. (1986). Drift vortices in a rotating magnetoplasma. *Physics of Fluids*, **29**, 1739–1740.

Shukla, P. K., Yu, M. Y., and Varma, R. K. (1985). Drift-Alfven vortices. *Physics of Fluids*, **28**, 1719–1721.

Stern, M. E. (1975). Minimal properties of planetary eddies. *Journal of Marine Research*, **33**, 1–13.

Verkley, W. T. M., (1989). On atmospheric blocking and the theory of modons. Ph.D. Thesis, Vrije Universiteit te Amsterdam.

Yu, M. Y. and Lisak, M. (1986). Dipole vortex solutions of magnetohydrodynamic equations describing microturbulence. *Physics of Fluids*, **29**, 143–145.

Zabusky, N. J. and McWilliams, J. C. (1982). A modulated point vortex model for geostrophic, beta-plane dynamics. *Physics of Fluids*, **25**, 2175–2182.